DRAFT VERSION NOVEMBER 12, 2021
Typeset using LaTeX default style in AASTeX631

Toward Improved Understanding of Magnetic Fields Participating in Solar Flares: Statistical Analysis of Magnetic Field within Flare Ribbons

MARIA D. KAZACHENKO,[1,2] BENJAMIN J. LYNCH,[3] ANTONIA SAVCHEVA,[4,5] XUDONG SUN,[6] AND BRIAN T. WELSCH[7]

[1]*Dept. of Astrophysical and Planetary Sciences, University of Colorado Boulder, 2000 Colorado Ave, Boulder, CO 80305, USA*
[2]*National Solar Observatory, 3665 Discovery Drive, Boulder, CO 80303, USA*
[3]*Space Sciences Laboratory, University of California, Berkeley, CA 94720, USA*
[4]*Harvard-Smithsonian Center for Astrophysics, 60 Garden st., Cambridge, MA 02138, USA*
[5]*Institute of Astronomy and National Astronomical Observatory, Bulgarian Academy of Sciences, 72 Tsarigradsko Chaussee Blvd., 1784 Sofia, Bulgaria*
[6]*Institute for Astronomy, University of Hawaii at Manoa, 34 Ohia Ku St, Pukalani, HI 96768, USA*
[7]*Dept. of Natural & Applied Sciences, Univ. of Wisconsin - Green Bay, Green Bay, WI 54311, USA*

ABSTRACT

Violent solar flares and coronal mass ejections (CMEs) are magnetic phenomena. However, how magnetic fields reconnecting in the flare differ from non-flaring magnetic fields remains unclear owing to the lack of studies of the flare magnetic properties. Here we present a first statistical study of flaring (highlighted by flare-ribbons) vector magnetic fields in the photosphere. Our systematic approach allows us to describe key physical properties of solar flare magnetism, including distributions of magnetic flux, magnetic shear, vertical current and net current over flaring versus non-flaring parts of the active region, and compare these with flare/CME properties. Our analysis suggests that while flares are guided by the physical properties that scale with AR size, like the total amount of magnetic flux that participates in the reconnection process and the total current (extensive properties), CMEs are guided by mean properties, like the fraction of the AR magnetic flux that participates (intensive property), with little dependence on the amount of shear at polarity inversion line (PIL) or the net current. We find that the non-neutralized current is proportional to the amount of shear at PIL, providing direct evidence that net vertical currents are formed as a result of any mechanism that could generate magnetic shear along PIL. We also find that eruptive events tend to have smaller PIL fluxes and larger magnetic shears than confined events. Our analysis provides a reference for more realistic solar and stellar flare models. The database is available online and can be used for future quantitative studies of flare magnetism.

Keywords: Sun: flares – Sun: magnetic fields – Sun: active regions

1. INTRODUCTION

Solar flares and coronal mass ejections (CMEs) that produce the most severe space weather disturbances arise from significant reconfiguration of magnetic fields in the solar corona. Because these coronal fields are rooted in the underlying, much-denser solar photosphere, understanding how flares and CMEs work requires understanding the structure and evolution of magnetic fields from the photosphere to the corona. Historically, most of the analyses of photospheric magnetic fields before and during the flares focused on the active region (AR) as a whole (e.g. Toriumi & Wang 2019). However, flare observations have shown that only a fraction of the AR magnetic field participates in the flare – from the analysis of 3000 solar flares we found that the

maria.kazachenko@colorado.edu

fraction of active-region magnetic flux that undergoes reconnection ranges from $(3 \pm 2)\%$ to $(21 \pm 10)\%$ for C1 to X-class flares, respectively (see Fig. 11 in Kazachenko et al. 2017). Moreover, subsequent flares can occur in very different areas of the same AR – a well-known example is the two extreme events on 2003 October 28 and 29 that occurred in different locations in AR 10486 (Kazachenko et al. 2010). This implies that to understand why and how flares occur, we need to understand the properties of the magnetic fields that participate in the flare and also how they differ from the AR as a whole.

According to the canonical, two-dimensional (2D) flare model called the CSHKP model (Carmichael 1964; Sturrock 1968; Hirayama 1974; Kopp & Pneuman 1976) and its extension to 3D (Longcope et al. 2007; Aulanier et al. 2012; Janvier et al. 2014; Savcheva et al. 2015, 2016), maps of flare ribbons identify footpoints of newly-reconnected magnetic fields (see Figure 1). In relation to magnetic topology, ribbons correspond to locations where separatrices, dividing domains of distinct connectivity, like spines and fans (Longcope et al. 2007; Kazachenko et al. 2012) or quasi-separatrix layers (QSL, Savcheva et al. 2015, 2016) intersect with the chromosphere. Until recently, limited accuracy of both vector-magnetic-field and ribbon measurements made systematic analysis of magnetic fields within flare ribbons areas limited.

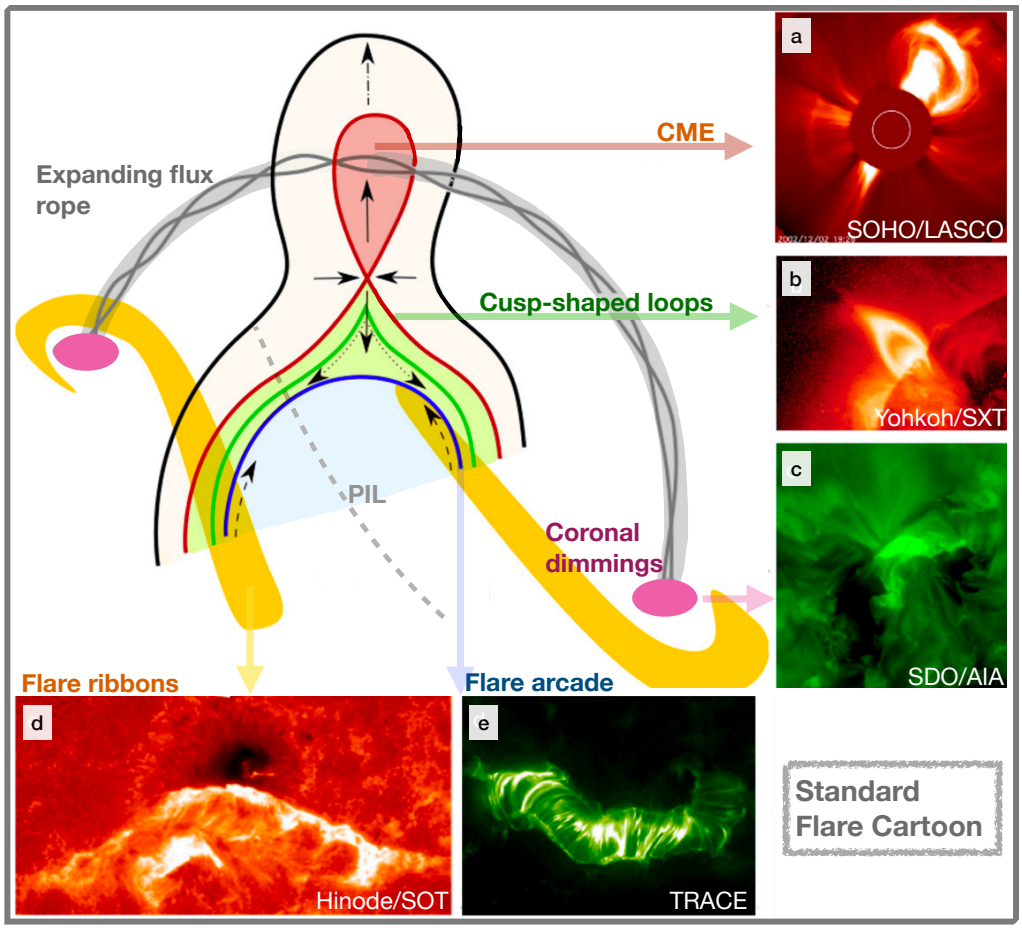

Figure 1. Standard flare cartoon from Savcheva et al. (2016). As the flux rope rises (gray), it stretches the current sheet and the QSLs in the plane perpendicular to the flux rope (red) forming a set of newly reconnected cusped and arcade-shaped field lines (green and blue, respectively) with footpoints, highlighted as flare ribbons (yellow). Images on the right and bottom show the main observed features explained by the model: (a) CME with three-part structure from SOHO/LASCO; (b) cusped loops from Yohkoh/SXT; (c) coronal dimmings from SDO/AIA; (d) flare ribbons from Hinode/SOT; and (e) flare arcade from TRACE. Published with the author's permission.

The launch of the *Solar Dynamics Observatory* (SDO; Pesnell et al. 2012), with the Helioseismic and Magnetic Imager (HMI; Scherrer et al. 2012; Hoeksema et al. 2014) and the Atmospheric Imaging Assembly (AIA; Lemen et al. 2012) instruments, marks the first time when both a vector magnetograph and ribbon-imaging capabilities became available on the same observing platform, making co-registration of AIA and HMI full-disk data relatively easy. In this paper, we make use of these two instruments and present a database of vector magnetic field properties swept by flare ribbons in 40 flaring events, C-class and larger. Our intentions are twofold. First, we provide the reference information for the data set by describing the key processing procedures. Second,

we present statistical analyses of the photospheric magnetic field participating in the flare and their relationship with that of the polarity inversion line (PIL) and the AR as a whole.

This paper follows the study of Kazachenko et al. (2017) that presented a RibbonDB database of 3137 solar flare ribbon events, their ribbon area and ribbon magnetic fluxes (reconnection fluxes). Complementing our previous study, here we create a new dataset, FlareMagDB, and describe the vector magnetic fields properties: magnetic flux, mean magnetic shear, vertical current and the net current within flare ribbons, AR and PIL areas.

This paper is organized as follows. In §2, we describe the SDO data we use, the list of selected events, and the methods. In §4, we describe statistical results of the FlareMagDB analysis. In §5, we describe the results of the analysis of the 3D MHD ARMS simulation. Finally, in §6 and §7, we discuss the results and summarize conclusions.

2. DATA AND METHODS

In this section, we describe the data and the methods we used to identify various physical properties of the AR magnetic field: identification of the polarity inversion line (PILs), flare ribbons and AR areas; estimates of the magnetic fluxes, shears, vertical currents and net currents within PIL, ribbons and AR areas.

2.1. *Data*

We have assembled a FlareMagDB catalogue that includes 40 flares: 10 X-, 28 M- and 2 C-class flares (see Table 1). To give an overview of these 40 events, in Figure 2 we show vertical magnetic field maps of 40 ARs hosting these flares. Out of 40 events, 33 were associated with CMEs (eruptive) and 7 were not associated with CMEs (confined, 2 C-, 2 M- and 3 X-class flares, Yashiro et al. 2006). To select our 40 events we used the RibbonDB flare ribbon catalogue that described reconnection flux properties of 3137 flares (Kazachenko et al. 2017). Our main selection criteria was choosing a sample of events spanning a wide range of AR and reconnection fluxes of flare class M1.0 and above, representative of the medium and strong flares of the RibbonDB catalogue. Figure 3 compares FlareMagDB events with events from the RibbonDB: it shows scatter plots of the peak X-ray flux vs. unsigned AR, ribbon and PIL magnetic fluxes for events in both databases.

For each event in the database, we use 1) a pre-flare HMI/SDO vector magnetogram of $ds_{\rm HMI} = 0.5''$ spatial resolution, $\mathbf{B}(x,y) = (B_x, B_y, B_z)(x,y)$, to find magnetic field properties before the flare and 2) a sequence of AIA 1600Å images, of $dt_{1600} = 24$s cadence and $ds_{1600} = 0.''61$ angular resolution, $I_{1600}(x,y,t)$, to find areas that have been swept up by flare ribbons during the course of the flare (i.e. cumulative ribbon masks, see Kazachenko et al. 2017). For the magnetic field we used a full-disk vector magnetogram data set from the 135-seconds series (Sun et al. 2017, hmi.B_135S). To disambiguate the azimuth orientation of the magnetic field we used the radial acute disambiguation method (Hoeksema et al. 2014). We process the UV 1600Å images in IDL using the aia_prep.pro SolarSoft package and co-align the AIA image sequence in time with the first frame. We use aia_prep.pro to align HMI vector magnetic fields maps with the AIA image sequence. In all magnetic field calculations, we set to zero the components of the vector magnetic field $\mathbf{B}$, where $|B_z| < 20G$. This noise threshold is chosen experimentally to remove areas outside the AR (Hoeksema et al. 2014). For finding PILs, we first smooth the input magnetic field with a Gaussian function with a window size of 2 pixels, then isolate areas where vertical magnetic field $|B_z| > 200G$ and finally dilate areas of positive and negative flux with a window size of 8 pixels. This procedure results in PILs that are roughly 8 AIA pixels or $\approx$ 3500km wide. We notice that some of the derived PILs are not directly related to the flaring regions – there are few false PILs in the isolated-sunspots penumbra and also PILs that lie away from the flares; however the areas and fluxes of these PILs do not contribute significant amounts of flux in our analysis and we thus do not exclude them. To account for noise in the weak transverse component of $\mathbf{B}$, we set $(B_x, B_y) = 0$, where $|B_h| < 200G$. We define the AR region-of-interest (ROI) as a 800×800-pixels, or a $390'' \times 390''$, rectangle centered on the AR. We chose the rectangle big enough to include the AR as a whole and small enough to exclude neighboring ARs. We derive the coordinates of the AR center from the Heliophysics Event Catalogue (HEC) maintained by the INAF-Trieste Astronomical Observatory.

2.2. *Methods: Analyzed physical variables*

We use HMI/SDO photospheric vector magnetic field maps in Cartesian coordinates, $\mathbf{B}(x,y) = (B_x, B_y, B_z)(x,y)$, to find the following pre-flare magnetic field properties: the potential component of the magnetic field, $\mathbf{B}^{\rm p} = (B^{\rm p}_{\rm x}, B^{\rm p}_{\rm y}, B_{\rm z})$, the magnetic shear, $\alpha(x,y)$ (Petrie 2019; Wang et al. 2017; Gosain & Venkatakrishnan 2010) and the vertical electric current density, $J_{\rm z}(x,y)$ (Liu et al. 2017):

$$\alpha(x,y) = |B| cos^{-1}\left(\frac{\mathbf{B}\cdot\mathbf{B}^p}{BB^p}\right) = |B|\theta, \tag{1}$$

$$J_{\rm z}(x,y) = \frac{1}{\mu_0}\nabla\times B_h = \frac{1}{\mu_0}\left(\frac{\partial B_y}{\partial x} - \frac{\partial B_x}{\partial y}\right). \tag{2}$$

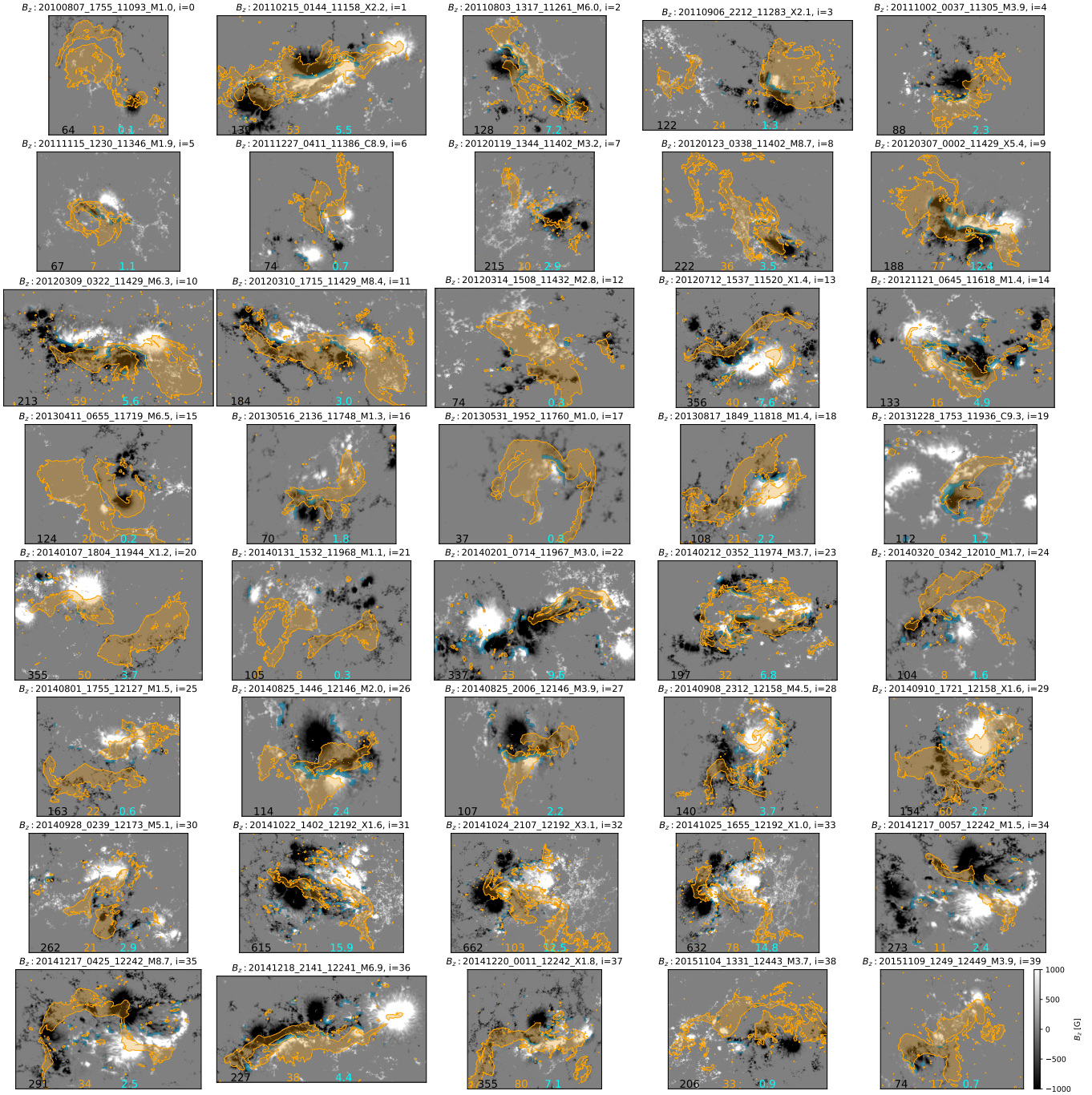

Figure 2. Vertical magnetic field maps, B_z, for 40 events from the FlareMagDB database. Cyan color shows PIL areas. Orange color shows cumulative ribbon areas. Labels above each figure combine event's index in the database, flare start time, NOAA active region number and the GOES peak X-ray flux. "Eruptive/confined" label indicates whether the event is eruptive or confined. Black, orange and cyan numbers indicate total magnetic flux within AR, ribbon and PIL areas, respectively, in units of 10^{20} Mx (see column Φ in Table 1). Here and in Figures 11 and 12, we zoom into the ROI's field-of-view to highlight the AR structure.

To calculate the potential field $\mathbf{B}^{\mathrm{p}}$, we used the poloidal-toroidal decomposition of the photospheric vector magnetic field (see Appendix A in Fisher et al. 2010).

From the above quantities we then find the following area-integrated physical quantities: the unsigned and the averaged between positive and negative magnetic fluxes (Φ_u and Φ), the total area (S), the mean shear ($\bar{\alpha}$), and the unsigned vertical current ($I_{\mathrm{z,u}}$):

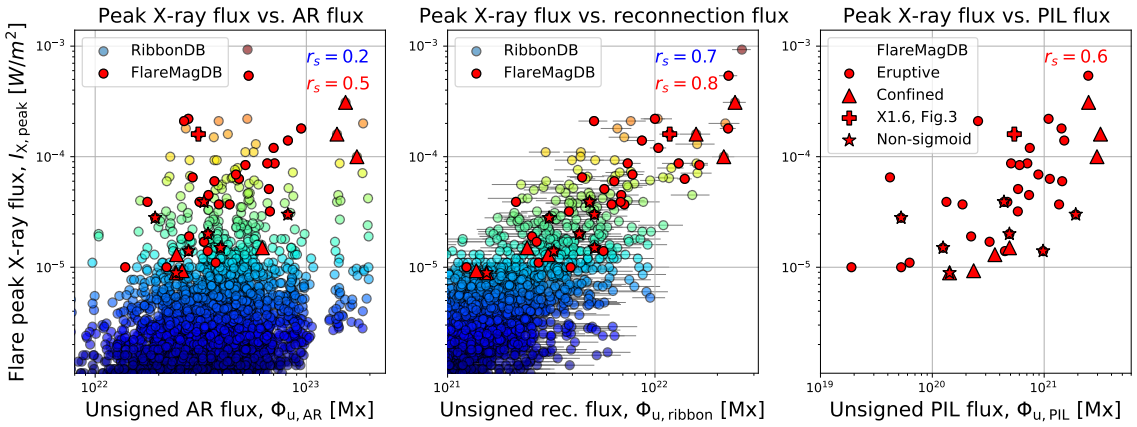

Figure 3. Comparison of FlareMagDB (red) vs. RibbonDB (rainbow) flare samples: scatter plots of peak X-ray flux vs. unsigned pre-flare AR magnetic flux (*left*), flare reconnection flux (*middle*) and flux within the PIL (*right*). *Rainbow color* shows peak X-ray fluxes of events from the RibbonDB database; it varies from blue for C-class flares to orange for X-class flares. *Red color shows* a subset of 40 FlareMagDB events. A "+"-sign indicates the example X1.6 event in AR 12158 (see Figure 4.1); △ show 7 non-CME events. Stars show events that do not exhibit sigmoidal structure in EUV images. See §2.

$$\Phi_u = \int |B_n|\, dS, \qquad S = \int dS, \tag{3}$$

$$\Phi = \frac{\left|\int\limits_{B_z>0} B_z dS\right| + \left|\int\limits_{B_z<0} B_z dS\right|}{2} = \frac{|\Phi_+| + |\Phi_-|}{2}, \tag{4}$$

$$\bar{\alpha} = \frac{\frac{\int\limits_{B_z>0} \alpha dS}{S_+} + \frac{\int\limits_{B_z<0} \alpha dS}{S_-}}{2} = \frac{\bar{\alpha}_+ + \bar{\alpha}_-}{2}, \tag{5}$$

$$I_{z,u} = \frac{\int\limits_{B_z>0} |J_z| dS + \int\limits_{B_z<0} |J_z| dS}{2} = \frac{|I_{z,u+}| + |I_{z,u-}|}{2}, \tag{6}$$

where dS is the area of integration and "+" and "−" subscripts refer to integration over positive and negative polarities, respectively. To describe physical quantities within PIL, ribbon and AR areas we separately integrate over three areas of interest (dS): area of the active region (AR, $|B_z| > 20G$), area swept by the flare ribbons (rbn, $|B_z| > 20G$) and area within the magnetic polarity inversion line (PIL). We only consider areas where $|B_h| > 200G$ to calculate $\bar{\alpha}$ and $I_{z,u}$.

In addition to describe the fraction of the AR undergoing magnetic reconnection, we use the percentage of the ribbon-to-AR magnetic fluxes as first described in Kazachenko et al. (2017):

$$R_\Phi = \frac{\Phi_{\rm ribbon}}{\Phi_{\rm AR}} \times 100\%. \tag{7}$$

To estimate the net current we follow the steps below. We first integrate J_z values of different signs in each polarity separately and compute the direct (DC) and return (RC) currents in each polarity (Liu et al. 2017; Schmieder & Aulanier 2018). To associate the correct sign of J_z to the DC (and hence to the RC), we find the dominant sign of helicity, H, handedness/sign (or J_z/B_z) of the AR as a whole. To define handedness we use orientation of the coronal loops from the coronal images relative to the field orientation of the AR from the magnetogram. Knowing the correct sign for DC (and RC), we then calculate DC and RC in positive and negative polarities, ($|DC|^+$ and $|RC|^+$) and ($|DC|^-$ and $|RC|^-$), respectively. For right-handed AR with positive helicity ($H > 0$):

$$DC^+ = \int\limits_{B_z>0, J_z>0} J_z\, dS, \quad RC^+ = \int\limits_{B_z>0, J_z<0} J_z\, dS, \tag{8}$$

$$DC^{-} = \int\limits_{\mathrm{B_z<0,J_z<0}} J_z \, dS, \quad RC^{-} = \int\limits_{\mathrm{B_z<0,J_z>0}} J_z \, dS, \tag{9}$$

For left-handed AR with negative helicity ($H < 0$):

$$DC^{+} = \int\limits_{\mathrm{B_z>0,J_z<0}} J_z \, dS, \quad RC^{+} = \int\limits_{\mathrm{B_z>0,J_z>0}} J_z \, dS, \tag{10}$$

$$DC^{-} = \int\limits_{\mathrm{B_z<0,J_z>0}} J_z \, dS, \quad RC^{-} = \int\limits_{\mathrm{B_z<0,J_z<0}} J_z \, dS. \tag{11}$$

From the above direct and return currents in positive and negative polarities, we determine the net current (or an in inverse of neutralization ratio defined in Dalmasse et al. 2015):

$$\left|\frac{DC}{RC}\right| = \frac{\frac{|DC^{+}|}{|RC^{+}|} + \frac{|DC^{-}|}{|RC^{-}|}}{2}. \tag{12}$$

$\left|\frac{DC}{RC}\right|$ describes current neutralization within the region of interest, an active region as a whole (AR) or reconnected field lines connecting flare ribbons (ribbon).

To describe CMEs associated with the eruptive events in the `FlareMagDB`, we include CME speeds from Yashiro et al. 2006 catalog.

2.3. *Methods: Uncertainties*

To estimate the uncertainties in the observed quantities in Eqs. 4-12, we calculate their differences within positive ("+") and negative ("−") magnetic polarities. Since for an isolated active region opposite polarities correspond to the footpoints of a single magnetic flux system, estimates within opposite polarities should be equal within the observational errors.[1] Adopting this hypothesis, we define the error proxies for signed magnetic fluxes, mean shears, total vertical currents and the net currents in the following way:

$$\Delta\Phi = \frac{|\Phi_{+}| - |\Phi_{-}|}{2}, \qquad \Delta\bar{\alpha} = \frac{|\bar{\alpha}_{+}| - |\bar{\alpha}_{-}|}{2}, \tag{13}$$

$$\Delta I_z = \frac{|I_{z,u+}| - |I_{z,u-}|}{2}, \qquad \Delta\left|\frac{DC}{RC}\right| = \frac{\frac{|DC^{+}|}{|RC^{+}|} - \frac{|DC^{-}|}{|RC^{-}|}}{2}. \tag{14}$$

From the way we construct these metrics we expect that for ideal measurements these error proxies should be zero.

2.4. *Statistical Analysis*

To quantitatively describe the relationship between different properties of flares and ARs, e.g. $\mathbb{X}$ and $\mathbb{Y}$, we use Spearman ranking correlation coefficient, $r_s(\mathbb{X}, \mathbb{Y})$ (see Figure 5). Unlike the Pearson correlation coefficient that is used to measure *linear* relationship between variables—and therefore is not optimal for non-linearly related variables—the Spearman rank correlation provides a measure of a *monotonic* relationship between variables. We describe the qualitative strength of the correlation using the following guide for the absolute value of r_s (Kazachenko et al. 2017): $r_s \in [0.2, 0.39]$ – weak, $r_s \in [0.4, 0.59]$ – moderate, $r_s \in [0.6, 0.79]$ – strong, and $r_s \in [0.8, 1.0]$ – very strong. When the correlation coefficient is moderate or greater ($r_s(\mathbb{X}, \mathbb{Y}) > 0.4$), we fit the relationship between $\mathbb{X}$ and $\mathbb{Y}$ with a power-law function

$$\mathbb{Y} = a\mathbb{X}^{b} \, . \tag{15}$$

We use Levenberg-Marquardt non-linear least-squares minimization method to find the scaling factor a and exponent b.

[1] We note that our shear parameter does not obey any conservation principle. Also, our PIL algorithm does not enforce balance in either flux or current. Nonetheless, we do not expect substantial imbalances in these quantities, so it is plausible to use excursions from zero in these quantities to indicate large uncertainties, perhaps arising from systematic effects.

3. RESULTS

4. RESULTS: OBSERVATIONAL ANALYSIS OF THE DATASET

In this section we first show results of the magnetic field analysis within PIL, ribbon and AR areas for an example AR 12158 (§4.1, Figure 4). We then describe results of the statistical analysis for 40 events of the `FlareMagDB`: magnetic flux (§4.2), flux ratio (§4.3), magnetic shear (§4.4) and total and net currents (§4.5). Table 1 contains the list of all the variables for 40 events. Table 2 and Figure 5 show variables' typical range and correlation matrix between 18 `FlareMagDB` variables.

4.1. *FlareMagDB example event: X1.6 flare in AR 12158*

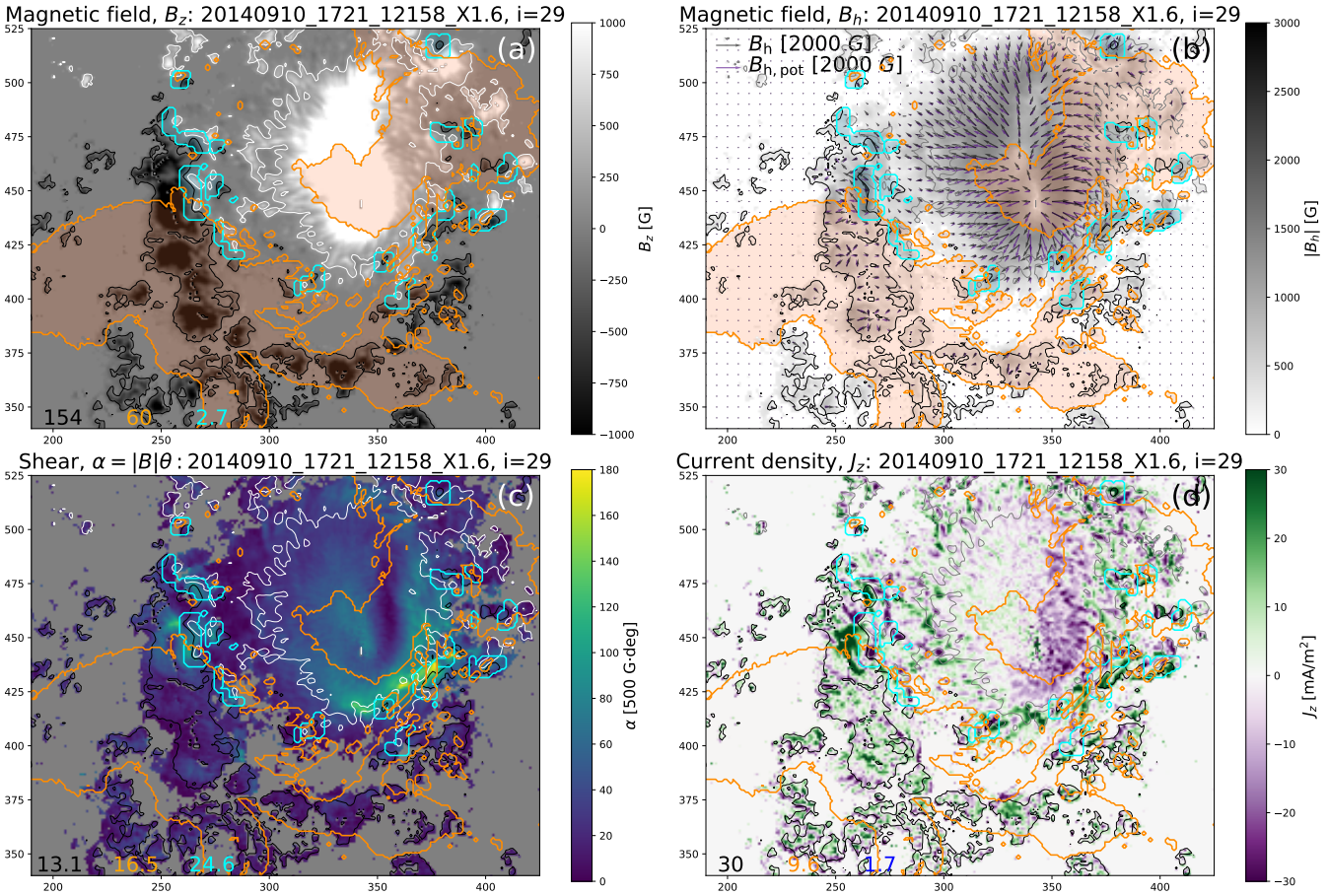

Figure 4. Example of an X1.6 flare on September 10 2014 in AR 12158 from the FlareMagDB database: clockwise from upper left, vertical and horizontal components of the magnetic field, magnetic shear and the vertical current density before the flare. Orange and blue contours outline ribbon and PIL areas, respectively. Black and blue arrows show observed and potential components of the horizontal magnetic field. See §4.1.

Figure 4 shows an example of our analysis for one event in the `FlareMagDB` database, an X1.6 flare on September 10 2014 in AR 12158 (event number $i = 29$ in Table 1). Four panels show vertical and horizontal magnetic field components, shear and current density maps right before the flare. Orange contours indicate areas swept by the flare ribbon. Cyan contours show locations of the PILs. In Table 1 we show the results of the quantitative analysis for this event (marked with "+") and all the other `FlareMagDB` events. From the magnetic flux analysis we find that the AR magnetic flux is $\Phi_{\rm AR} = 154 \times 10^{20} Mx$, the magnetic flux swept by flare ribbons is $\Phi_{\rm rbn} = 60 \times 10^{20} Mx$, and the PIL magnetic flux is $\Phi_{\rm PIL} = 2.7 \times 10^{20} Mx$ (Figure 4a). We find that the mean shear is largest within the PIL area gradually decreasing within the ribbon and AR areas ($\bar{\alpha}_{\rm PIL} = 24.6 \times 10^3 G \cdot deg$ vs. $\bar{\alpha}_{\rm ribbon} = 16.5 \times 10^3 G \cdot deg$ and $\bar{\alpha}_{\rm AR} = 13.1 \times 10^3 G \cdot deg$), which corresponds to field being increasingly sheared as we go from AR to ribbon and PIL areas. In 4(c) we can see this transition from the most yellow, or largest-shear areas, near the cyan PILs to bluer, i.e smaller-shear areas, outside the ribbon and PIL contours in the AR as a whole (Figure 4b,c). As for the

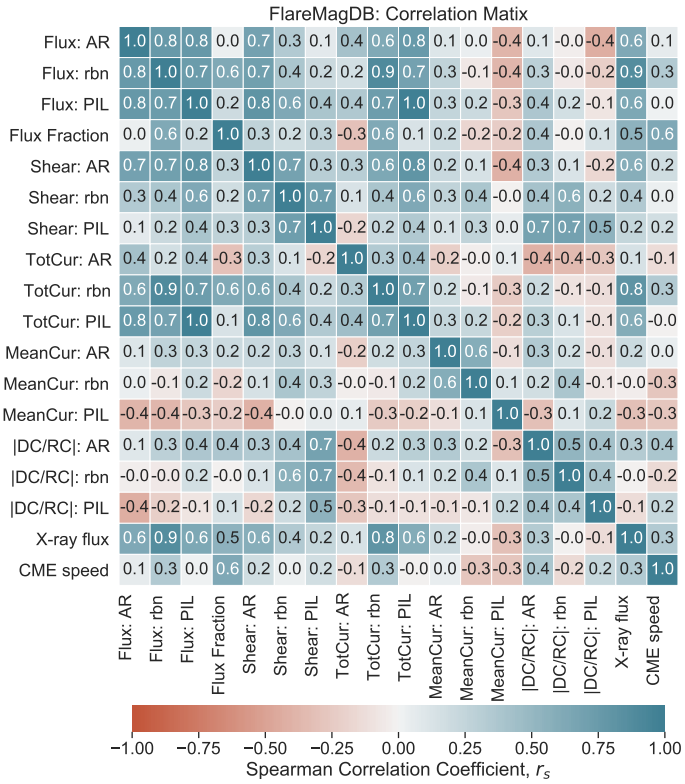

Figure 5. *FlareMagDB Correlation matrix:* Spearman correlation coefficients, r_s, between variables of FlareMagDB, $\mathbb{X}$. Here $\mathbb{X}$ is either magnetic flux, ribbon-to-AR fraction of magnetic flux, mean magnetic shear, total current, mean current, net current within AR, ribbon and PIL areas, GOES peak X-ray flux or CME speed. Colors correspond to the strength of the correlation coefficient, r_s, between each variable pair. We verbally describe the strength of the correlation using the following guide for the absolute value of r_s: $r_s = [0.2, 0.39]$ – weak, $r_s = [0.4, 0.59]$ – moderate, $r_s = [0.6, 0.79]$ – strong and $r_s = [0.8, 1.0]$ – very strong correlation.

net vertical current, that describes current neutralization, we find that the current is non-neutralized within separate polarities, increasing from AR to PIL areas: $|DC/RC|[\mathrm{AR}, \mathrm{rbn}, \mathrm{PIL}] = [1.2, 1.6, 1.6]$. In 4d we see this current imbalance as preferred current colors in opposite magnetic polarities – notice how current is more violet within positive ribbon (orange contour in the top right) and more green within negative ribbon (bottom left).

4.2. *FlareMagDB Statistics: Magnetic flux*

Figure 2 shows vertical magnetic field maps, $B_z(x, y)$, of 40 events in the `FlareMagDB` database. Does the geometry of PIL affect where flare ribbons of the next flare would be? Does a stronger PIL necessarily mean that the flare ribbons of the next flare would lie close to PIL? According to the standard flare model, ribbons should never cross PILs and should lie on both sides of the PIL at a distance defined by the reconnection process and the structure of the pre-flare coronal magnetic field. We examine spatial distribution of cyan and orange contours showing PIL and ribbon areas (see Figure 2). We find that ribbons and PIL-masks generally sample different parts of the ARs. For example, for the 10 strongest flares, X-class and above, only 3 X-class flares have ribbons lying close to strong PIL areas ($i = 1, 3, 9$). In the other 7 X-class flares, ribbons lie away from strong PIL areas ($i = 13, 20, 29, 31, 32, 33, 37$). From this comparison we conclude that while large amounts of near-PIL flux indicate a large flare is more likely, the morphology of PILs has almost *no bearing* on the morphology of flare ribbons. We then use these $B_z(x, y)$ maps to find unsigned and averaged between opposite polarities vertical magnetic fluxes, Φ_u and Φ (Eq. 3-4), for each event within the AR, ribbon and PIL areas (see contours).

Figure 3 shows scatter plots of pre-flare *unsigned* magnetic fluxes, Φ_u (see Eq. 3), within AR, reconnection and PIL area vs. peak X-ray flux for each event in the `FlareMagDB` database. Rainbow color corresponds to events from the 3137-flares `RibbonDB` catalogue ($n = 3137$, Kazachenko et al. 2017). Red color shows a subset of 40 `FlareMagDB` events selected in this

Table 1. FlareMagDB database: magnetic field properties of 40 flares within AR, ribbon and PIL areas. H, Φ, $\bar{\alpha}$, $I_{z,u}$, $|DC/RC|$ and V_{CME} refer to AR handedness, magnetic flux, mean magnetic shear, total, net currents and CME speed, respectively. $\triangle$s mark confined events. "+' marks an example event (§4.1). See §4 for details.

i	T_{start}	Flare	AR	H	$\Phi, 10^{20} Mx$			$\bar{\alpha}, 10^3 G \cdot deg$			$I_{z,u}, 10^{12} A$			$\lvert DC/RC \rvert$			V_{CME}
		class	number	+/-	AR	rbn	PIL	AR	rbn	PIL	AR	rbn	PIL	AR	rbn	PIL	km/s
00	2010-08-07 17:55	M1.0	11093	-1	64	12	0.1	8.4	12.0	11.0	45	4.8	0.0	1.0	1.3	1.9	871
01	2011-02-15 01:44	X2.2	11158	1	139	53	5.5	12.8	25.1	51.5	49	13.8	3.6	1.1	1.5	1.7	669
02	2011-08-03 13:17	M6.0	11261	1	127	23	7.2	11.9	18.5	34.5	61	9.5	5.7	1.2	1.6	4.2	610
03	2011-09-06 22:12	X2.1	11283	1	122	23	1.3	7.8	20.9	41.7	48	7.7	0.8	1.1	2.0	3.2	575
04	2011-10-02 00:37	M3.9	11305	-1	87	10	2.3	7.7	16.3	34.9	37	3.6	1.5	1.2	2.0	2.8	259
05	2011-11-15 12:30	M1.9	11346	-1	67	06	1.1	7.4	15.1	19.2	123	5.5	1.1	1	1.8	1.9	300
06$^{\triangle}$	2011-12-27 04:11	C8.9	11386	1	74	04	0.7	7.7	10.5	13.1	170	3	0.8	1.1	1.0	1.6	-
07	2012-01-19 13:44	M3.2	11402	-1	215	10	2.9	10.7	17.9	21.8	230	5.0	2.6	1.0	1	1.2	1120
08	2012-01-23 03:38	M8.7	11402	-1	222	35	3.5	10.7	16.9	21.2	160	18.2	3.3	1.0	1.1	2.1	2175
09	2012-03-07 00:02	X5.4	11429	-1	188	76	12.4	14.3	29.3	41.3	124	27.2	7.7	1.1	1.6	2.0	2684
10	2012-03-09 03:22	M6.3	11429	-1	212	59	5.6	12.3	19.1	43.1	99	14.7	3.4	1.2	1.8	4.4	950
11	2012-03-10 17:15	M8.4	11429	-1	184	58	3.0	12.9	18.8	32.5	87	19.0	2.4	1.2	1.4	2.3	1379
12	2012-03-14 15:08	M2.8	11432	1	74	12	0.3	7.9	10.8	9.1	30	3.5	0.2	1.0	1.1	0.7	411
13	2012-07-12 15:37	X1.4	11520	1	356	40	7.6	15.5	22.1	29.4	94	6.6	3.9	1.2	1.7	1.9	885
14	2012-11-21 06:45	M1.4	11618	-1	132	15	4.9	11.4	23.5	30.0	37	4.3	3	1.2	2.3	2.4	410
15	2013-04-11 06:55	M6.5	11719	-1	123	19	0.2	8.3	12.6	11.7	52	4.9	0.2	1.0	1.1	1.8	861
16$^{\triangle}$	2013-05-16 21:36	M1.3	11748	-1	69	07	1.8	8.9	16.9	25.0	85	5.0	1.5	1.0	1.8	2.5	-
17	2013-05-31 19:52	M1.0	11760	-1	37	03	0.3	7.0	16.4	37.6	95	2.8	0.3	1.0	1.3	2.7	388
18	2013-08-17 18:49	M1.4	11818	1	108	20	2.2	10.1	24.1	61.9	89	6.3	1.2	1.1	1.9	4.9	1202
19$^{\triangle}$	2013-12-28 17:53	C9.3	11936	-1	112	06	1.2	8.2	17.9	25.5	37	2.1	0.7	1.0	2.8	2.8	-
20	2014-01-07 18:04	X1.2	11944	1	355	50	3.7	9.6	10.1	21.8	77	9.4	2.2	1.1	1.1	1.7	1830
21	2014-01-31 15:32	M1.1	11968	-1	105	07	0.3	8.3	11.3	8.8	123	5.5	0.3	1.0	0.9	1.7	462
22	2014-02-01 07:14	M3.0	11967	-1	336	23	9.6	14.4	23.6	34.4	133	7.2	7.1	1.1	1.7	1.0	-
23	2014-02-12 03:52	M3.7	11974	-1	196	32	6.8	8.6	17.0	24.9	69	11.8	4.5	1.0	1.3	1.2	373
24	2014-03-20 03:42	M1.7	12010	1	103	07	1.6	8.1	14.5	15.0	83	3.5	1.5	1.0	0.8	1.9	740
25	2014-08-01 17:55	M1.5	12127	1	162	21	0.6	9.3	12.5	12.0	69	6.0	0.5	1.0	1	1.1	789
26	2014-08-25 14:46	M2.0	12146	-1	114	13	2.4	11.1	25.9	38.2	59	5.9	1.7	1.1	2.4	1.5	555
27	2014-08-25 20:06	M3.9	12146	-1	106	13	2.2	9.8	28.0	35.0	74	6.1	1.9	1.1	2.0	2.0	711
28	2014-09-08 23:12	M4.5	12158	-1	140	28	3.7	13.1	21.5	25.6	65	6.3	2.8	1.2	1.4	1.3	920
29^{+}	2014-09-10 17:21	X1.6	12158	-1	154	60	2.7	13.1	16.5	24.6	30	9.6	1.7	1.2	1.6	1.6	1267
30	2014-09-28 02:39	M5.1	12173	-1	262	21	2.9	10.4	17.5	21.2	137	8.0	2.8	1.0	1.8	1.0	215
31$^{\triangle}$	2014-10-22 14:02	X1.6	12192	-1	614	70	15.9	13.2	21.3	20.2	192	17.4	10.8	1.0	1.2	0.9	-
32$^{\triangle}$	2014-10-24 21:07	X3.1	12192	-1	661	102	12.5	13.2	18.2	19.5	209	29.3	9.2	1.0	1.1	0.8	-
33$^{\triangle}$	2014-10-25 16:55	X1.0	12192	-1	632	77	14.8	13.0	21.5	20.1	350	24.0	11.0	1.0	1.2	0.8	-
34$^{\triangle}$	2014-12-17 00:57	M1.5	12242	1	273	10	2.4	11.1	20.5	24.4	147	3.4	2.0	1.0	1.8	1.0	-
35	2014-12-17 04:25	M8.7	12242	1	290	34	2.5	12.5	18.1	27.4	89	6.1	2.0	1.1	1.9	0.9	587
36	2014-12-18 21:41	M6.9	12241	1	227	37	4.4	9.9	18.2	33.4	62	9.0	2.8	1.2	2.6	1.3	1195
37	2014-12-20 00:11	X1.8	12242	1	354	80	7.1	11.5	19.9	25.5	161	30.5	5.1	1.1	1.2	1.7	841
38	2015-11-04 13:31	M3.7	12443	1	206	33	0.9	7.0	7.8	20.4	40	6.1	0.7	1.0	1.2	0.7	578
39	2015-11-09 12:49	M3.9	12449	1	73	17	0.7	8.4	15.6	11.3	125	9.5	0.5	1.0	0.9	0.9	1041
i	T_{start}	Flare	AR	H	$\Phi, 10^{20} Mx$			$\bar{\alpha}, 10^3 G \cdot deg$			$I_{z,u}, 10^{12} A$			$\lvert DC/RC \rvert$			V_{CME}

Table 2. Typical range of active-region, flare-ribbon and PIL properties, $\mathbb{X}$, for 40 events of FlareMagDB database and ARMS simulation. $\mathbb{X}$ is either magnetic flux Φ, ribbon-to-AR fractions of magnetic flux R_Φ, mean magnetic shear $\bar{\alpha}$, total unsigned current $I_{z,u}$, or net current $|DC/RC|$. We describe the typical range of each quantity as the 20^{th} to 80^{th} percentile, $\mathbb{X}[P_{20}, P_{80}]$. For more details see Figures 6-7.

	OBSERVATIONS (FlareMagDB)			**SIMULATIONS (ARMS)**		
Quantity	Typical range, $\mathbb{X}[P_{20}, P_{80}]$			$\mathbb{X}_{\rm ARMS}$		
$\mathbb{X}$	AR	Ribbon	PIL	AR	Ribbon	PIL
Magnetic Flux, Φ $[10^{20} Mx]$	$[100, 276]$	[10,54]	[0.9,6.9]	41	18	0.3
Reconnection flux fraction, R_Φ [%]	-	[8.3,20.1]	-	-	43	-
Mean Magnetic Shear, $\bar{\alpha}$ $[10^3 G \cdot deg]$	[8.2,12.9]	[14.2,21.7]	[18.3,34.9]	0.06	0.13	0.17
Total Current, $I_{z,u}$ $[10^{12} A]$	[50,139]	[4.7,14]	[0.7,4.0]	0.3	0.2	0.003
Net Current, $|DC/RC|$ [-]	[1.0,1.16]	[1.1,1.9]	[1.0,2.4]	4.9	10.5	3.1

paper. For events from the `FlareMagDB` we find a moderate correlation between the unsigned AR flux and the flare peak X-ray flux. This correlation is stronger than the correlation found for `RibbonDB`: Spearman correlation coefficient $r_s = 0.5$ for $n = 40$ vs. $r_s = 0.2$ for $n = 3137$ (left plot). We also find a strong correlation between the unsigned reconnection flux and the flare peak X-ray flux: $r_s = 0.8$ for $n = 40$ vs. $r_s = 0.7$ for $n = 3137$ (middle plot). We explain the difference in correlation coefficients between a subsample of $n = 40$ events and the full sample of $n = 3137$ by the high heterogeneity of the full `RibbonDB` dataset. We also note that using H_α dataset from the Kanzelhohe Observatory instead of the AIA/SDO observations, Tschernitz et al. 2018 found stronger correlations ($r_s = 0.9$) in agreement with our findings here. Finally, we find a strong correlation between the PIL vertical magnetic flux and the flare peak X-ray flux: $r_s = 0.6$ (right plot).

In Figure 6a we show AR, ribbon and PIL magnetic fluxes averaged between opposite polarities, Φ vs. the peak X-ray flux for the `FlareMagDB` alone (see Eq. 4). By definition, these averaged fluxes are around 2-times smaller than unsigned fluxes from Figure 3. We find that the flare size is moderately correlated with the AR magnetic flux and the strength of the PIL and very strongly correlated with the amount of reconnecting magnetic flux. In Table 2 we describe the typical range of AR, ribbon and PIL fluxes consistent with earlier results (Kazachenko et al. 2017).

In Figure 5 we show the Spearman correlation coefficients between AR, ribbon and PIL fluxes and other `FlareMagDB` variables, the correlation matrix. We find very strong correlations ($r_s > 0.8$) between magnetic flux and total current within PIL. Note that PIL and AR fluxes have weaker correlation with the Peak X-ray flux than the ribbon reconnection flux. We discuss these relationships further in §6.

4.3. *FlareMagDB Statistics: Reconnection Flux Fraction*

In Figure 6b we show the fraction of the magnetic flux participating in the flare, R_Φ (see Eq 7) vs. the peak X-ray flux. We find that R_Φ has a moderate correlation with the peak X-ray flux ($r_s = 0.5$). The reconnection flux fraction has the typical range of 8.3% to 20.1%, consistent with previous results (Kazachenko et al. 2017).

4.4. *FlareMagDB Statistics: Magnetic Shear*

Figure 11 in Appendix A shows magnetic shear maps, $\alpha(x, y)$, for all events of the database. From these maps we find that the spatial structure of the magnetic shear highly varies for different events. To understand these variations in a quantitative way, we use individual shear maps to find the mean magnetic shear, $\bar{\alpha}$, within the AR as a whole, ribbon and PIL areas (see Eq. 1).

Figure 6c shows the mean magnetic shear vs. the peak X-ray flux. We find that the mean magnetic shear in AR, ribbon and PIL areas is $[10, 18, 26] \times 10^3 G \cdot deg$ with the 20^{th} to 80^{th} percentile of $[8.2, 12.9] \times 10^3 G \cdot deg$, $[14.2, 21.7] \times 10^3 G \cdot deg$ and $[18.3, 34.9] \times 10^3 G \cdot deg$, respectively (see Table 2). In other words, as we go from the AR as a whole to ribbon and PIL areas, the magnetic field becomes stronger and more sheared. In addition, we find that the peak X-ray flux has a strong correlation with the mean magnetic shear within the AR and weak to moderate correlations with the mean magnetic shear within PIL and ribbon areas.

4.5. *FlareMagDB Statistics: Vertical Current and Net Current*

Figure 12 in Appendix A shows vertical current density maps, $J_z(x, y)$, for all events of the database. Zooming in into individual J_z images, we see that the vertical current density consists of long and short structures, or "threads" and "patches", of violet

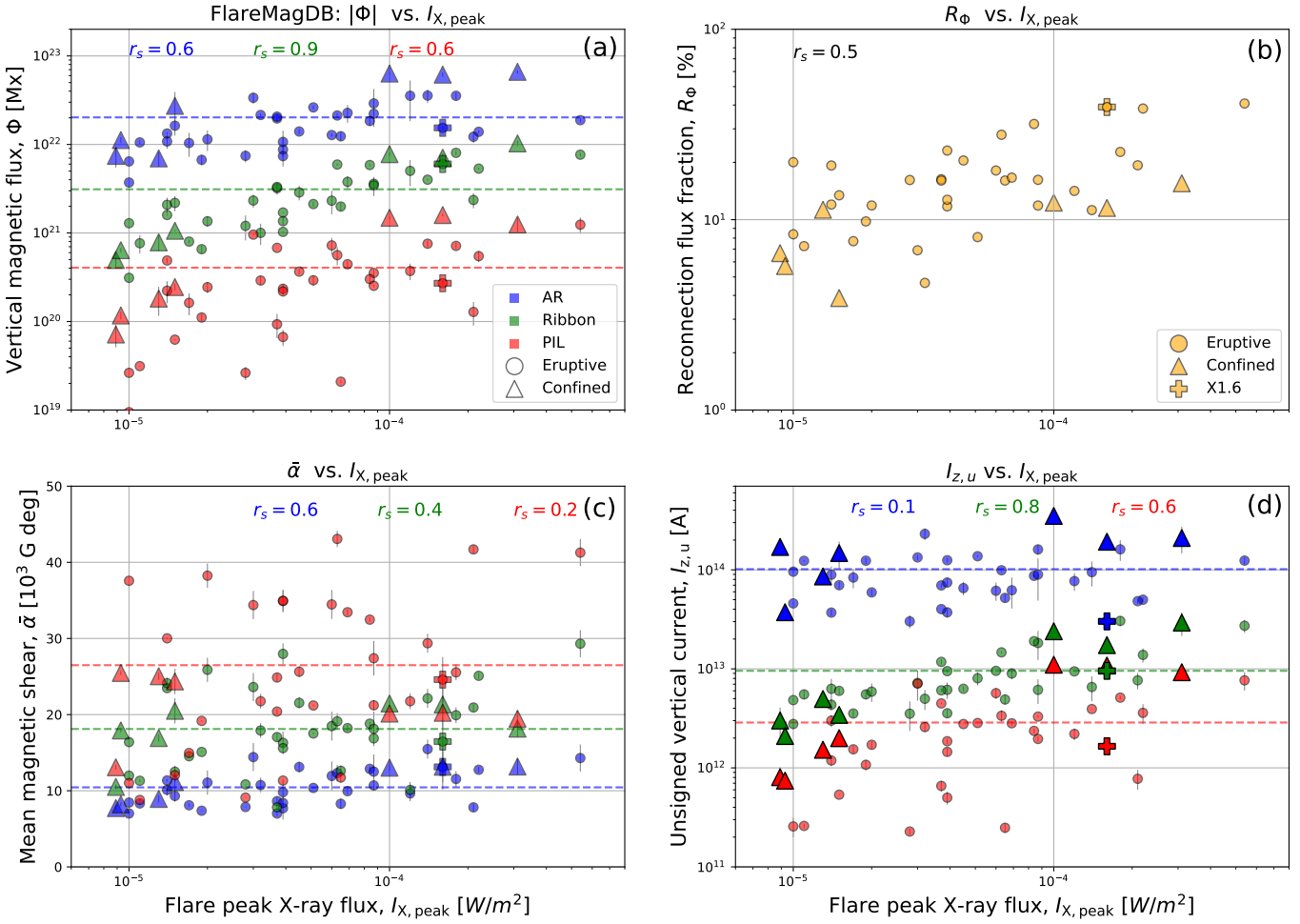

Figure 6. *FlareMagDB results*: magnetic field properties for 40 events of FlareMagDB database. Vertical magnetic flux (*top left*, §4.2), reconnection flux fraction (*top right*, §4.3), mean magnetic shear (*bottom left*, §4.4) and the total unsigned vertical current (*bottom right*, §4.5) vs. the peak X-ray flux within AR, ribbon and PIL areas. The error bars correspond to error proxies as defined in §2.3.

and green colors that correspond to positive and negative vertical currents. While we find elongated thread structures in some events, e.g. events $i = 1$ (`01_20110215_0144_11158_X2.2`), $i = 22$ (`22_20140201_0714_11967_M3.0`) or $i = 36$ (`36_20141218_2141_12241_M6.9`), from our limited sample we do not find any relationship between the presence of these structures and occurrence of large flares or CMEs (see e.g. a non-thread-like event `29_2014_0910_1721_12158_X1.6`, where an X1.6 occurred with a CME). Instead we find that the current density maps have all kinds of shapes of varying size that are not related to flare size or flare/CME productivity.

To quantify the global properties of J_z, we use J_z maps to compute the total unsigned vertical current, $I_{z,u}$, direct current (DC), return current (RC) and their ratio, or net current, $|DC/RC|$ as described in Eqns. 6-12.

Figure 6d shows the scatter plot between the total unsigned vertical current and the peak X-ray flux before the flare within PIL, ribbon and AR areas. We find that the total unsigned vertical current is largest within AR areas decreasing gradually within ribbon and PIL areas. This relationship is not surprising and reflects the decreasing area of integration as we go from AR to ribbon and PIL areas. Comparing Figure 6a and Figure 6d, i.e. the vertical-magnetic-flux and the total-vertical-current scatter plots, we see similar scattering with the peak X-ray flux. The Spearman correlation coefficient between the peak X-ray flux and the total vertical current ranges from weak for ARs to strong for ribbon and PIL areas.

In Figure 7 we describe the imbalance of the vertical current within each magnetic polarity, *the net current*, in AR, ribbon and PIL areas and compare these to various magnetic field properties. Our objective here is to understand the cause of the net current. In Figure 7a we compare the $|DC/RC|$ with the peak X-ray flux. We find that $|DC/RC|$ and the flare peak X-ray flux have

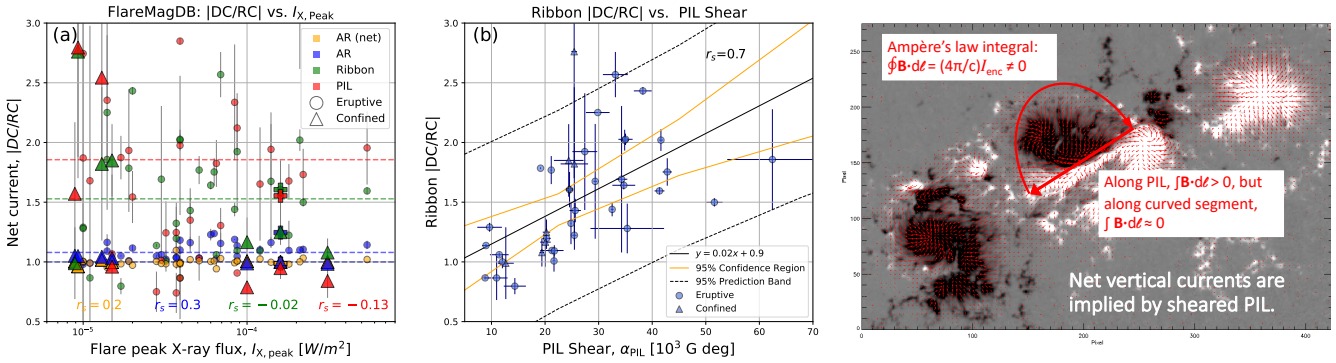

Figure 7. *FlareMagDB results*: net current properties for 40 events of FlareMagDB database. *Left panel, (a):* DC/RC vs. the peak X-ray flux; *Middle panel, (b):* DC/RC within ribbons vs. mean PIL shear angle. The error bars correspond to error proxies as defined in §2.3. *Right panel*: explanation of the scaling law in Panel (b), between the net current and shear at PIL, as a consequence of the Ampère's Law. See §4.5.

weak correlation, implying that the net current is not related to how large the next flare might be. We find that the net current is larger within PILs, than within ribbons and separate AR polarities ($\overline{|DC/RC|} = [1.1, 1.5, 1.7]$ within ARs, ribbons and PILs, respectively), i.e. the current is more non-neutralized within ribbons' than within AR's polarities. If we look not at the separate polarities but at the AR as a whole, we find that $|DC/RC| \approx 1$, i.e the current is neutralized.

To understand the cause of the net current, in Figure 7b we compare the pre-flare mean shear with the net current within flare ribbons. We find a strong correlation between the net current within ribbons and the mean shear within the PIL. Using a linear function we find the $(13 \pm 3)x + (6 \pm 5)$ relationship between the two and a Spearman correlation coefficient of 0.7. We find a similar relationship between the AR net current and the PIL shear, with a slightly weaker correlation coefficient. What does this relationship imply? It implies that the net current is a manifestation of the magnetic shear at the PIL.

4.6. *FlareMagDB Statistics: Confined vs. Eruptive Events*

We analyze magnetic field properties of 7 *confined* events, that did not cause CMEs (marked with △s in Figure 6 and Figure 7), and compare them with 33 *eruptive* events, that caused CMEs (marked with •s). 7 confined events originated in 5 ARs, including 3 X-class flares, $X3.1$, $X1.6$ and $X1.0$, originating in the AR 12192 (Sun et al. 2015).

Comparing confined vs. eruptive events, we find several differences in their magnetic field properties. First, we find that for flares within a certain peak-X-ray-class range, confined events have larger PIL magnetic fluxes than eruptive events (Figure 6a). Second, we find that confined events have smaller PIL-shear and ribbon net current than eruptive events (cf. △ vs. •). Third, we find that the reconnection flux fraction, R_Φ, tends to be smaller for confined events than for eruptive events (Figure 6b). If we look at eruptive events alone, we find that their reconnection flux fractions strongly correlate with the CME speeds, $r_s(r_\Phi, v_{\rm CME}) = 0.6$. In fact, among all `FlareMagDB` variables, it is the reconnection flux fraction that has the strongest correlation with the CME speed. In Figure 8 we plot the CME speed vs. the `FlareMagDB` variables that have the highest correlation coefficients with the CME speed, peak X-ray flux, AR net current and the reconnection flux fraction. To summarize, we find that while PIL shear and the net current have weak to moderate correlation with the CME speed, the reconnection flux fraction has a strong correlation with the CME speed, i.e. the properties of the field of the flux rope play smaller role in the CME speed that the properties of flux rope relative the overlying field.

We note that our analysis of field properties within confined and eruptive events is based on 33 eruptive and only 7 confined events. Analysis of a larger data sample with equal numbers of confined and eruptive events would be necessary to draw more certain conclusions.

5. *RESULTS: 3D MHD ARMS SIMULATIONS*

To provide theoretical ground for our observational findings, here we present the same observational analysis on the results of a 3D MHD simulation of an idealized magnetic breakout CME (Antiochos et al. 1999; Lynch et al. 2008) that forms a large-scale post-eruption arcade below an energetic flux rope (FR) eruption. We note, that while the simulation's AR magnetic flux is similar to a flux of the medium active region, the mean magnetic field strengths (and AR size) are about 100 times smaller (larger) in the simulations than observed. Using the scaling law between the reconnection flux and the peak X-ray flux, we conclude that the simulation's reconnection flux corresponds to an M1.0-class flare.

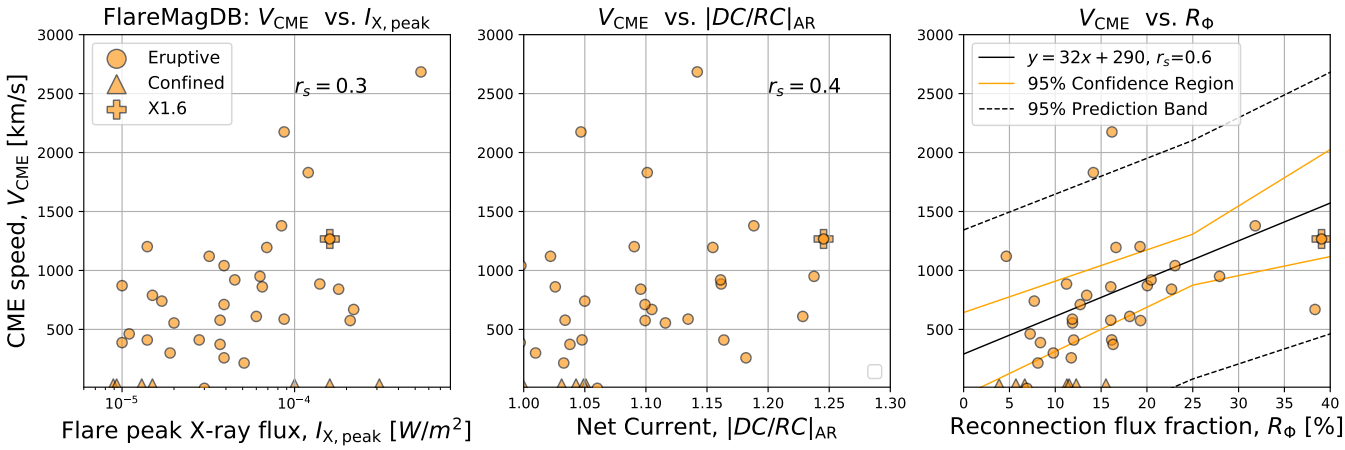

Figure 8. *FlareMagDB results*: CME speeds vs. highest-correlated flare magnetic properties, peak X-ray flux, AR net current and the reconnection flux fraction, for 33 eruptive (•) and 7 confined (△) flares of FlareMagDB database. See §4.6.

5.1. *Model Details and Initial Conditions*

The 3D MHD simulation was performed with the Adaptively Refined MHD Solver (ARMS; DeVore & Antiochos 2008). The simulation is a left-handed Lynch et al. (2009) configuration, energized with a pair of idealized shearing flows parallel to the active region PIL.

The magnetic field at $t = 0$ hr is initiated via a sum of point dipoles,

$$\mathbf{B}(\mathbf{r},0) = \sum_i M_i \left(\frac{R_i}{r'_i}\right)^3 \left[3\mathbf{n}_i\left(\mathbf{n}_i\cdot\mathbf{m}_i\right) - \mathbf{m}_i\right] , \tag{16}$$

where $r'_i = |\mathbf{r} - \mathbf{r}_{i,0}|$, $\mathbf{n}_i = \mathbf{r'}_i/r'_i$, and each dipole has a moment magnitude M_i, location $\mathbf{r}_{i,0}$, scaling factor R_i, and is pointing in the $\mathbf{m}_i$ direction. As in Lynch et al. (2009), $i = [1,\ 6]$, and the parameters used here are given in Table 3.

The base pressure and temperature are given by $p_0 = 0.025$ dyn cm^{-2} and $T_0 = 1.9433 \times 10^6$ K, respectively, while the initial solar atmosphere is in hydrostatic equilibrium with $p(r) = p_0\,(r/R_\odot)^{-\mu}$, $T(r) = T_0\,(r/R_\odot)^{-1}$, $p = 2(\rho/m_p)k_BT$, and $\mu = R_\odot/H_\odot = 12.0$ is the normalized (inverse) scale height. This yields a base mass density of $\rho_0 = 7.80 \times 10^{-17}$ g cm^{-3} corresponding to a base number density of $n_0 = 4.6634 \times 10^7$ cm^{-3}.

The computation grid is block decomposed with an initial resolution of $5 \times 5 \times 5$ blocks covering the full domain of $r \in [1R_\odot,\ 20R_\odot]$, $\theta \in [0.0625\pi, 0.9375\pi]$ (latitude of $\pm 78.75°$) and $\phi \in [-0.5\pi, +0.5\pi]$. Each block contains 8^3 grid cells and we have employed 4 additional levels of static grid refinement. The highest-refined region covers $r \in [1R_\odot,\ 6R_\odot]$, $\theta \in [0.32\pi, 0.55\pi]$ (latitude of $[-9.0°, +32.4°]$) and $\phi \in [-0.18\pi, +0.18\pi]$ with an effective resolution of 320^3. Thus, the highest-refined grid cells have a $0.49° \times 0.56°$ angular resolution in (θ, ϕ) and $\Delta r = 0.0188R_\odot$ at the lower boundary.

The energizing boundary flows impart a significant shear component (B_ϕ) to the active region as each polarity concentration is moved further apart. The form of the Lynch et al. (2009) shearing flows are

$$\mathbf{v}_h^{(\pm)} = \pm v_0 f^{(\pm)}(\theta,\phi)\left(\frac{1}{2} - \frac{1}{2}\cos\left[\frac{2\pi t}{(10^4\ \mathrm{s})}\right]\right)\hat{\phi}\ , \tag{17}$$

where $(\pm)$ represents the flows applied to the positive and negative polarities, respectively, for the duration $t \in [0, 2.778]$ hr. The function $f^{(\pm)}(\theta, \phi)$ smoothly ramps the flow profile to zero outside of specified $(\theta,\ \phi)$ ranges on either side of the PIL, described in Lynch et al. (2009). The magnitude of the shearing flows $v_0 = 65$ km s^{-1} is significantly faster than observed photospheric velocities but below the sound speed ($c_0 \sim 180$ km s^{-1}) and extremely sub-Alfvénic ($v_A \gtrsim 2000$ km s^{-1}) in the vicinity of the AR.

5.2. *Eruption Details*

The magnetic breakout model for CME initiation relies on the positive feedback process associated with reconnection at a current sheet *above* the source region's expanding sheared core (Antiochos et al. 1999; Lynch et al. 2008). The arcade expansion

Table 3. ARMS initial magnetic field point dipole parameters

i	M_i [G]	R_i [$R_\odot$]	$\mathbf{r}_{i,0}$ ($r/R_\odot$, θ, ϕ)	$\mathbf{m}_i$ ($\hat{r}$, $\hat{\theta}$, $\hat{\phi}$)
1	1.00	1.0	(0, 0, 0)	(0, 1, 0)
2	0.08	1.0	(0.80, 0.45π, -0.025π)	(0, 1, 0)
3	0.08	1.0	(0.80, 0.45π, $+0.025\pi$)	(0, 1, 0)
4	0.10	0.33	(0.95, 0.45π, 0)	(0, 1, 0)
5	0.10	0.33	(0.95, 0.45π, -0.010π)	(0, 1, 0)
6	0.10	0.33	(0.95, 0.45π, $+0.010\pi$)	(0, 1, 0)

accelerates as the restraining over-lying flux is transferred into the adjacent arcades of the AR multipolar flux system. Reconnection at the breakout current sheet drives the initial stages of the eruption and leads to the transition from slow quasi-ideal evolution to a driven, runaway configuration that forms a vertical current sheet *below* the expanding sheared field core. This current sheet thins and elongates with continued expansion and, with the onset of the fast CSHKP eruptive flare reconnection, ushers in the explosive acceleration phase of the CME eruption (e.g. DeVore & Antiochos 2008; Karpen et al. 2012; Lynch & Edmondson 2013; Dahlin et al. 2019; Wyper et al. 2021).

Figure 9 shows a snapshot of the simulation results during the CME eruption. Panel 9a shows the field lines of the post-eruption flare arcade in the very beginning of the eruption ($t = 2.71$ hr), and panel 9b shows the temporal evolution of total magnetic energy, kinetic energy, flare reconnection flux, and reconnection rate. To focus on changes of the magnetic energy during the eruption we have set the magnetic energy at $t = 0$ to zero: $E_M(t = 0) = 0$. The amount of the total released magnetic energy, i.e. the E_M decrease from 2 to 5hr, is $\Delta E_M \sim 6 \times 10^{30}$ erg, which roughly corresponds to the change in the free magnetic energy. The kinetic energy exhibits two stages of evolution. During the initial stage from 1 hr to 2.6 hr the kinetic energy E_K increases slowly corresponding to a slow quasi-ideal rise of the sheared core before the onset of flare reconnection. This expansion is initially caused by the force imbalance (magnetic pressure gradient) introduced with the sheared field component. During the second runaway stage, from 2.6 hr to 5 hr, E_K increases much more rapidly corresponding to the start of the breakout reconnection. Once the flare reconnection starts, it becomes the dominant process driving the entire subsequent evolution of the CME eruption (Karpen et al. 2012). By the end of the flare at $t = 5$ hr, the kinetic energy reaches a maximum of $E_K \sim 10^{30}$ erg and the cumulative unsigned reconnection flux reached $\Phi_{\rm rbn} \sim 1.8 \times 10^{21}$ Mx. The maximum reconnection rate is $d\Phi_{\rm rbn}/dt \sim 5.5 \times 10^{17}$ Mx s^{-1} at $t = 2.85$ hr. The total fraction of the active region flux that participated in the flare is 43% (Table 2).

5.3. *Magnetic Field and Electric Current Properties in the AR, PIL, and Flare Ribbon Regions*

To apply the observational analysis framework to the simulation results, we first project the spherical magnetic field components into a Cartesian coordinate system where (x, y) represent the plane-of-the-sky (horizontal components) and z comes out of the page towards the observer (vertical component). Next, we interpolate the simulation values onto a uniform 600×500 array corresponding to the area shown in Figure 9a, i.e. $x \in [-0.6R_\odot, +0.6R_\odot]$, $y \in [-0.25R_\odot, +0.75R_\odot]$. This yields a pixel area $dA_{ij} = \Delta x \Delta y = 1.96 \times 10^{16}$ cm^2. From this data set, we calculate the magnetic shear $\alpha(x, y)$, vertical current density $J_z(x, y)$, and their respective averages over the regions of interest defined in Section 2.2.

Figure 10 shows the ARMS simulation version of Figure 4 at $t = 2.57$ hr, *right before the onset* of the fast eruptive-flare reconnection. Figures 10a, b show the vertical and horizontal field components with the cumulative, over the flare duration, ribbon and PIL areas denoted as the orange and cyan shading, respectively. Here the ribbon areas are calculated from a field line length proxy, as in Lynch et al. (2019, 2021). Figure 10c shows the distribution of shear and Figure 10d shows the distribution of the vertical current density.

Table 2 shows a comparison of observed values from `FlareMagDB` with ARMS. The mean magnetic flux in each region is $\Phi(AR, rbn, PIL) = [4.1, 1.8, 0.03] \times 10^{21}$ Mx. The mean shear in each region is $\bar{\alpha}(AR, rbn, PIL) = [63, 129, 169] \times (G \cdot deg)$. The total unsigned vertical current in each region is $I_{\rm z,u}(AR, rbn, PIL) = [2.7, 2.1, 0.03] \times 10^{11}$ A. The net current in each region is $|DC/RC|(AR, rbn, PIL) = (4.9, 10.5, 3.1)$. Comparing these values with observations, ARMS magnetic fluxes correspond to a medium-size flare in a medium-size active region. For example, an M1.0-class flare in a sigmoidal AR ($i = 0$) of

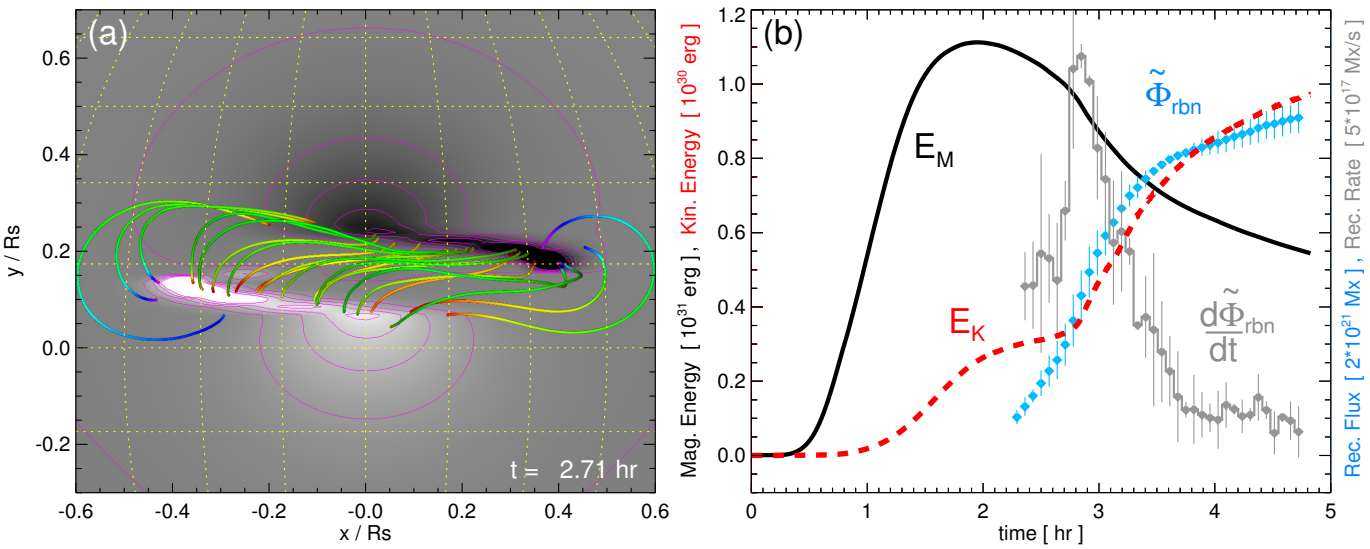

Figure 9. ARMS simulation results during the CME eruption: *Panel a*: radial magnetic field on the $r = R_\odot$ lower boundary with post-eruption arcade field lines at $t = 2.71$ hr. *Panel b*: total magnetic, $E_M(t) - E_M(0)$, and kinetic, $E_K(t)$, energies along with total unsigned reconnection flux ,$\Phi_{\rm rbn}$, and reconnection rate, $d\Phi_{\rm rbn}/dt$. See §5.2 for details.

`FlareMagDB` has very similar AR, ribbon and PIL magnetic fluxes. The size of the ARMS AR is much larger than any observed case, therefore the magnetic fields are much weaker. Since the magnetic fields are much weaker, ARMS magnetic shears (which is a product of the magnetic field magnitude and the shear angle, θ) and total currents are much smaller than the observed ones. We also find that ARMS AR has very weak return currents, resulting in large net currents, which vary from 5 for a single polarity to 10.5 within a flare ribbon. For comparison, the observed ARs have smaller net currents ranging from 1 to 3, i.e. the return currents in the observations are stronger. Note that before the eruption when we start shearing the arcade, there is direct current close to PIL and a clear return-current shell separating the sheared from un-sheared components along the quasi-separatrix layer. During the eruption the return current weakens as a result of peeling away of the outer layers of the expanding flux system via breakout reconnection.

To summarize, from ARMS analysis we find the following: (1) Similar to observations, simulations' mean magnetic shear increases gradually from AR to ribbon and PIL areas. Simulations' shear values are consistent with the observed ones, given 100-times scaling relation between mean magnetic fields. (2) Similar to observations, the vertical electric currents within individual polarities are highly non-neutralized, with the largest net currents located within areas involved in the eruption. Simulation's net currents are ≈ 5 times stronger than observed values. (3) We find a close spatial relationship between the simulation's magnetic shear at PIL and the net current, confirming the new net current-shear scaling law we find from the observations.

6. DISCUSSION

We used HMI/SDO photospheric vector magnetic field observations in 40 flares to assemble a `FlareMagDB` database with properties of magnetic fields within AR, flare ribbon and PIL areas. We analyzed pre-flare *observed* magnetic flux, reconnection fraction, magnetic shear, total electric current and net current for 40 events and compared these with flare X-ray peak flux (Figures 6 and 7) and CME speed (Figures 8). In Table 2 we summarized variables' typical range and compared these with synthetic variables from an MHD ARMS eruption simulation. In the Correlation Matrix in Figure 5 we investigated dependencies between the variables. In this section we describe how our results complement existing understanding of flare magnetism.

Ribbon vs. PIL Morphology: We compare spatial distribution of ribbons and PILs and find that many flares, including M5.0 and above, have ribbons lying away from the PIL. What does it imply? First, that for many events the morphology of PILs has almost *no bearing* on the morphology of flare ribbons. Second, that in these events low-lying magnetic fields that are rooted in the vicinity of the PIL area do not participate in the flare. How do these ideas fit within the contention that large near-PIL fluxes indicate that a large flare is more likely to occur (Schrijver 2007)? We explain this with the fact that the majority of events in our list, 33 out of 40, have sigmoidal coronal structure (Canfield et al. 2007; Savcheva et al. 2014). Sigmoid is a twisted FR embedded in a surrounding field. Savcheva et al. (2012a,b) analyzed the time-evolution of a sigmoid eruption and constructed a scenario for the onset of the CME in sigmoidal regions: the pre-existing FR can develop into a CME as a consequence of reconnection

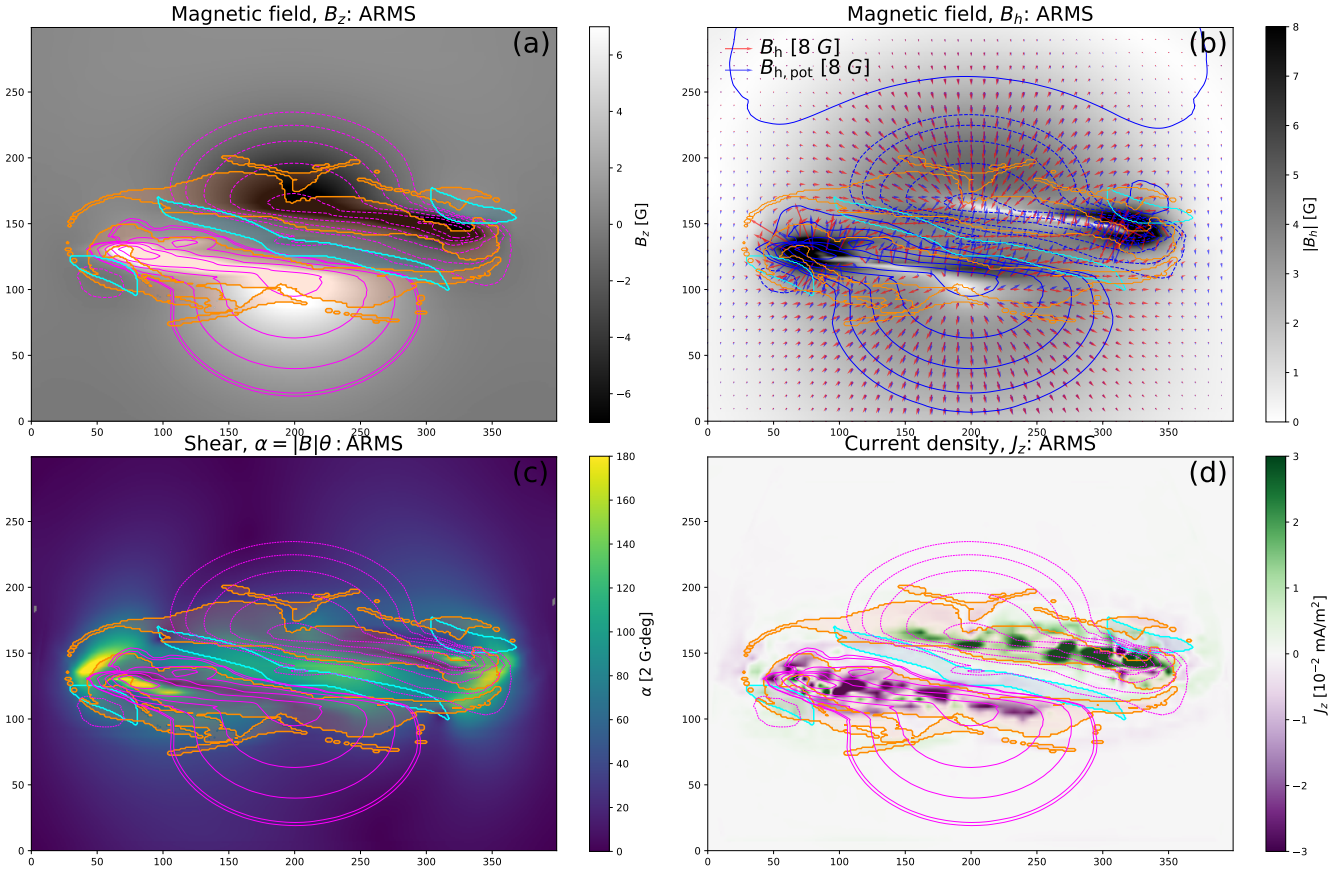

Figure 10. ARMS MHD quantities on the $r = R_\odot$ lower boundary analogous to those presented for an observed X1.6 flare in Figure 4. *Panel a*: vertical field B_z. *Panel b*: magnitude of the horizontal magnetic field and vector directions of the total and potential components (arrows). *Panel c*: distribution of magnetic shear $\alpha(x, y)$. *Panel d*: vertical current density $J_z(x, y)$. In each panel the total flare ribbon area during the eruption is denoted as the orange-shaded region while the cyan-shaded region indicated the AR PIL. See §5.3 for details.

at a Hyperbolic Flux Tube (HFT) under the FR, which increases the magnetic flux in the rope and at the same time weakens the overlying magnetic arcade holding it down. Thus, tether-cutting reconnection is needed in the slow rise phase of the eruption, and the torus instability is necessary to allow the CME eruption. On the other hand, presence of ribbons close to the PIL indicates of either the presence of a low-lying pre-existing flux rope or a creation of a FR during the flare as a result of the reconnection of the low-lying sheared magnetic fields (Kazachenko et al. 2012). A more detailed study of flare ribbon vs. PIL position and PIL properties relative to coronal structure would be helpful to advance our understanding of flux rope formation.

Magnetic flux: From the analysis of magnetic fluxes we find that ribbon and PIL fluxes have strong correlation with the AR flux, implying that large PIL and ribbon fluxes tend to occur in active regions with large magnetic fluxes. We also find that magnetic fluxes have moderate to strong correlation with other magnetic field products like mean magnetic shear and the total current. Specifically the correlation between the PIL flux and the AR shear is very strong ($r_s = 0.8$, see Correlation Matrix 5). One possible scenario to explain this relationship – as the active region evolves and gets pushed by photospheric flows, the AR field becomes more sheared and magnetic flux piles up at PIL due to, for example, collisional shearing (Chintzoglou et al. 2019).

We find strong correlation between the AR, ribbon and PIL magnetic fluxes and the peak X-ray flux ($r_s > 0.6$). While strong, correlation between the PIL flux and the X-ray peak flux is weaker than the correlation between the PIL flux and the AR flux ($r_s = 0.6$ vs. $r_s = 0.8$). In other words, while correlation between PIL flux and flare size is in line with Schrijver (2007) hypothesis that flare-productive ARs tend to have stronger PILs (see also references in Georgoulis et al. 2019), this correlation could reflect the fact that larger ARs have stronger PILs and hence host larger flares. A study of small vs. large active regions with the same amount of PIL flux might be useful to find out what plays the major role in the AR flare production, the AR flux or the PIL flux. We also find a very strong correlation between the reconnection flux and the peak X-ray flux ($r_s = 0.9$), in agreement with earlier results for larger datasets (Kazachenko et al. 2017; Toriumi et al. 2017; Tschernitz et al. 2018). The power law between the two quantities agrees with the Warren & Antiochos (2004) scaling from hydrodynamic simulations of

impulsively heated flare loops, proving that the soft X-ray radiation energy released during the flare comes from the free magnetic energy released during reconnection (Kazachenko et al. 2017).

Magnetic flux fractions: We find that fractions have a moderate correlation with the peak X-ray flux ($r_s = 0.5$) that is weaker than correlation between the ribbon flux and the peak X-ray flux. This result is in agreement with Kazachenko et al. (2017) ($r_s = 0.5$) and Toriumi et al. (2017). We explain this relationship as a consequence of the way how we calculate the fractions ($R_\Phi = \frac{\Phi_{\rm ribbon}}{\Phi_{\rm AR}} \times 100\%$) and a very strong correlation between the ribbon flux and the peak X-ray flux.

Mean magnetic shear: The amount of magnetic shear at PIL is known to be related to the flare productivity of an active region. Here, as noted above, we find that the amount of magnetic shear within the active region is most strongly correlated with the flux at PIL which in turn is strongly correlated with AR magnetic flux. The larger is the active region, the larger is the amount of shear it contains and more flux it has at PIL. Is the amount of shear related to flare peak X-ray flux? From our analysis, we find that it is not the case – mean magnetic shear has weak to moderate correlation with the peak X-ray flux that is weaker than the correlation between magnetic flux and the peak X-ray flux. For example, while PIL flux correlates with the flare size ($r_s = 0.6$), increased PIL shear does not correlate with AR flare size ($r_s = 0.2$). We also find that this correlation decreases from ARs to ribbons and PILs. As we go further from the PIL, we get less sheared magnetic fields, consistent with the standard 3D flare model (Janvier et al. 2014; Savcheva et al. 2016). Analysis of many large flares with large amount of PIL magnetic flux and small amount of shear at the PIL, such as for example an M8.7 flare ($i = 8$, $\Phi_{\rm PIL} = 21.2$) or an M6.5 ($i = 15$, $\Phi_{\rm PIL} = 11.7$) would be interesting.

In several past investigations and in ongoing work, Savcheva et al. (2015, 2016); Janvier (2016); Karna et al. (2021) have studied several of the active regions shown in Table 1, precisely, 2010-08-07 ($i = 0$), 2011-02-15 ($i = 1$), 2011-09-06 ($i = 3$), 2012-03-07 ($i = 9$), 2012-03-09 ($i = 10$), 2012-07-12 ($i = 13$), 2013-04-11 ($i = 15$) and 2014-10-22-25 ($i = 31, 32, 33$). Specifically, Savcheva et al. (2015, 2016) studied an M1.0 flare on 2010-08-07 (i=0) using a magnetofrictional (MF) evolution. They found that first reconnection happens under the flux rope turning two J-shaped field lines from the sheared arcade into an S-shaped field line that builds magnetic flux in the flux rope and produces flare field lines as a by-product. These flare field lines, that match the observed flare loops, initially lie close to the PIL and are highly sheared, carrying remnant shear of the flux rope shear, and sequentially, as the flux rope goes up in height, less and less sheared loops form that are rooted farther and farther away from the PIL (see cartoon in Fig 1. from Savcheva et al. 2016). This scenario, using MF simulation, supports data-constrained MHD simulation by Kliem et al. (2013) and also the observed large to small shear transition from PIL to ribbon areas that we find here.

Spatial structure of the vertical current density: What is the spatial structure of vertical current density and does it have any relationship with the ability of the AR to host a CME vs. a confined event? Recent works suggest that CME-eruptive ARs exhibit defined filamentary structures or ribbons in the current density maps while CME-quiet ARs do not (see e.g. Figure 3 of Avallone & Sun 2020). Some observed case studies and simulations suggested that a hook-shaped pattern in these filaments could be a signature of the pre-existing flux rope (Schmieder & Aulanier 2018; Janvier 2016; Barczynski et al. 2020). Do we see direct current ribbon pairs aligned with PIL before an AR hosts a CME (similar to the $q = 0.8$ case in Sun & Cheung 2021)? Do these current ribbons have hook shapes? To answer this question we examine `FlareMagDB` current density maps in Figure 12. First, we notice that few of these events have a clear hook shape. I.e. while hooks might be a signature of a pre-existing flux rope, hook presence is a rare phenomenon. Second, we find that while some eruptive events are associated with distinct current ribbon pairs close to PIL, others do not have these current ribbon pairs, instead consisting of salt-an-pepper patterns of positive and negative current density. For example, AR 11158 ($i = 1$, eruptive X2.2 flare) and AR 12241 ($i = 36$, eruptive M6.9 flare) have clear current ribbon pairs, while AR 11944 ($i = 20$, eruptive X1.2 flare) does not have current ribbons. Does it mean that eruptive events that do not have current ribbons are all in-situ formed flux ropes, i.e. flux ropes that were primarily formed during reconnection? Finally, we find that all seven confined events in our list do not have current ribbons. This result is consistent with earlier works and the scenario that lack of current ribbons might be related to absence of the pre-existing flux rope and as a result smaller likelihood of the flare to erupt. We conclude that a more detailed morphological study of J_z patterns in ARs hosting eruptive and confined events with analysis of pre-flare coronal images to track FR existence is needed to clarify the relationship between J_z morphology and the AR ability to erupt.

We also calculate the total and mean vertical current within AR, ribbon and PIL areas. We find that the total vertical current increases as we go from PIL to AR areas, reflecting larger integration areas. On the other hand, the mean current decreases from PIL to AR areas, since within PIL and ribbon areas magnetic fields are much more non-potential than in the AR as a whole.

Net current within AR, ribbons and PILs: Understanding how currents are neutralized is important for numerical models of solar eruptions (see introduction in Török et al. (2014) paper). If we look at the AR as a whole, we find that $|DC/RC| \approx 1$, i.e the current is neutralized, in agreement with previous studies (Wheatland 2000; Venkatakrishnan & Tiwari 2009; Georgoulis et al. 2012b). On the other hand, individual polarities contain a net current. This net current varies from 1 to 3 and is largest in

the central part of the active region, around PIL and ribbon areas, decreasing gradually within the polarity as a whole (an AR net current). In the simulations, net currents are larger but exhibit similar growth from the periphery to the center of the AR. For example, using ARMS simulations, here we find net currents reaching up to 5 within individual AR polarities and 10 within the ribbon areas. For a simulation of an emerging active region, Török et al. (2014) found net currents reaching up to 5, increasing as an AR emerges, consistent with pre-flare ARMS values. Titov et al. (2008) and Aulanier et al. (2010) in their MHD simulations also found weak return currents with net currents around 3, similar to observed values we find here with `FlareMagDB`.

What creates these net currents? Net currents could emerge bodily into the corona ("emergence", e.g. Leka et al. 1996; Longcope & Welsch 2000) or be produced by stressing of the coronal magnetic field by sub-photospheric and photospheric shearing flows ("shear", e.g. McClymont & Fisher 1989; Török & Kliem 2003; Aulanier et al. 2010). From our statistical analysis we find that the net current within each AR polarity (or ribbons) is proportional to magnetic shear at PIL, with most of the direct current lying in the PIL vicinity. In other words, net current is a manifestation of the magnetic shear at the PIL. This conclusion is in agreement with recent findings using simulations (Dalmasse et al. 2015; Török et al. 2014) and one-case *morphological* studies using observations (Ravindra et al. 2011; Georgoulis et al. 2012a; Vemareddy 2015; Liu & Schuck 2012). Török et al. (2014); Dalmasse et al. (2015) found that net currents are co-temporal with surge of shear at PIL and can be formed due to flux emergence, twisting and shearing motions and any mechanism that can generate magnetic shear along a PIL. Using high-resolution vector magnetograms from the Spectropolarimeter/Hinode instrument of an emerging AR over several days, Ravindra et al. (2011) noticed that net current within individual polarities could be related to shear at PIL. In a different study, Venkatakrishnan & Tiwari (2009) found that non-sheared PILs have zero net current. In this paper we perform a first *quantitative* analysis of a fairly large observations dataset and find that the net current is proportional to shear at PIL. This finding is expected from the integral form of the Ampère's law, $\oint \mathbf{B} \cdot dl = (4\pi/c)I$. While along the PIL $\oint \mathbf{B} \cdot dl > 0$, along the curved segment away from the PIL, $\oint \mathbf{B} \cdot dl \approx 0$. The presence of net current in our sample of ARs supports previous studies that state that return currents get trapped under the photosphere during flux emergence, leading to the presence of a net current causing increased shear at PIL. Our results also confirm that coronal flux rope models that neglect return currents are a valid representation of pre-eruption configurations on the Sun.

Confined vs. eruptive flares: Here we find that for a given X-ray flux, confined flares have smaller reconnection flux fractions, R_Φ, (cf. $\triangle$ vs. $\bullet$ in Fig. 6b). If we go one step further and look not just at the flare eruptivity, but at the CME speeds, we find that among all magnetic variables of `FlareMagDB`, reconnection flux fraction is the only variable that has a strong correlation with the CME speed ($r_s = 0.6$, see Correlation Matrix 5). Earlier, some indications of this relationship were suggested by Tschernitz et al. (2018) and Toriumi et al. (2017); Li et al. (2020). Tschernitz et al. 2018 analyzed 51 flares (32 confined, 19 eruptive) ranging from GOES class B3 to X17. They found that confined flares of a certain GOES class have smaller ribbon areas, but larger mean magnetic fields. This result implies that confined flares occur closer to the flux-weighted center of ARs, where fields that could be swept by the flare ribbons could be stronger. In a different study, Toriumi et al. (2017); Li et al. (2020) compared R_Φ in confined vs eruptive flares, finding that eruptive events have on average larger flux fractions. Here, instead of a binary comparison between confined and eruptive events properties, we for the first time analyzed the CME speed. In Figure 8 we show the scatter plot of the CME speed vs. the reconnection fraction with the functional fit of $y = ax + b$ describing the relationship, where $a = 32 \pm 9$ and $b = 290 \pm 180$ and $R^2 = 0.3$. If correct, the new relationship between the CME speed and the reconnection fraction could in principle be used to predict the CME speed once the solar flare occurs.

How could we explain the correlation between the CME speed and the reconnection flux fraction? We suggest the following scenario. Once the flare starts, reconnection starts feeding magnetic flux into a pre-existing flux rope or a sheared arcade. As this new flux rope forms, overlying fields within an AR provide a retrieving force to keep this flux rope stable. As a result the larger is the reconnection flux fraction, the weaker is the restraining arcade above and the faster the new flux rope erupts reaching torus instability at a lower height (Chen et al. 2019; Kliem et al. 2021). The torus instability occurs when the overlaying potential arcade decays with a critical index, $n_{\rm crit} = -\frac{dlnB}{dlnz} \approx 1.1 - 1.5$, depending on the flux rope geometry and shear in the overlaying arcade Kliem & Török (2006). If the tension of the arcade above is not sufficient, the flux rope starts expanding, thinning the reconnection current sheet further and causing more reconnection to take place. This scenario accounts for the slow rise of filaments based on tether-cutting-like reconnection (Moore et al. 2001) and the fast eruption after the torus instability kicks in. It is also in line with a recent observation analysis by Li et al. (2020); Li et al. (2021) who analyzed 322 and 719 flares, respectively, and found that the flare-CME association rate decreases with the increasing magnetic flux of the AR that produces the flare, implying that large magnetic flux tends to confine eruptions.

Physically reconnection flux fraction represents the ratio between the flux gained by the non-potential flux rope to the total more potential flux of the active region. Lin et al. (2021) generalized this idea calling it "relative non-potentiality" of a magnetic flux

rope. Consistent with the scenario above, a larger relative non-potentiality indicates a higher probability for a flux rope to erupt. §1 of Lin et al. (2021) contains a nice overview of a variety of schemes to quantitatively evaluate the relative non-potentiality.

We find that all of the confined events in our dataset have reconnection flux fraction, $R_\Phi < 15\%$, below the instability criteria, $R_{\Phi,\rm inst} \approx 30\%$, determined by the use of the flux rope insertion method (Savcheva & van Ballegooijen 2009; Savcheva et al. 2012; Su et al. 2011). (For comparison, the typical 20^{th} to 80^{th} percentile for the reconnection flux fraction in `FlareMagDB` is $R_\Phi[P_{20}, P_{80}] = [8.2, 20.1]\%$ and the ARMS value is $R_\Phi \approx 43\%$). On the other hand, as seen from the CME speed vs. reconnection flux fraction plot in Figure 8, there are many events that are eruptive and yet have the reconnection flux fraction below the instability criterion, $R_{\Phi,\rm inst} \approx 30\%$. A systematic analysis of these outlier events would be interesting to understand why these events are eruptive.

Compared to eruptive events, we find that confined events tend to have stronger PIL fluxes. We speculate that for a constant amount of flux in the flux rope, stronger vertical PIL flux implies weaker horizontal flux and as a result smaller magnetic energy within a flux rope.

We also compare PIL shear (and a related ribbon net current) for confined vs. eruptive events and find that confined events have smaller PIL-shear and ribbon net current. This result statistically confirms earlier studies of Liu et al. (2017) (4 events), Avallone & Sun (2020) (30 events) and Kontogiannis et al. (2019) (32 events) who found that flare-active/CME-active ARs are associated with larger net currents than flare-quiet/CME-quiet ARs. For our limited dataset, however, this relationship is not very strong with large number of outliers, i.e. there are many eruptive events with small net current, as has been previously noted by Avallone & Sun (2020). Case studies of these events might be useful to understand the relationship between eruptivity and the net current. From the physics standpoint, we explain the lack of shear in confined events by a smaller non-potential energy and hence a smaller likelihood to erupt.

We note that all our conclusions regarding confined vs. eruptive events are limited by a small number of confined events that we analyzed (7 events). Extension of this work to a larger sample of confined and eruptive events would be necessary to draw more confident conclusions.

7. CONCLUSIONS

In this paper we analyzed the pre-flare vector magnetic fields within *AR, flare ribbons and PIL* areas in 40 events and ARMS eruption simulation with an objective of improving our understanding of the physical properties of flaring vs. non-flaring photospheric vector magnetic fields in the photosphere.

Our quantitative findings are as follows:

- *Ribbon vs. PIL morphology:* Qualitatively, comparing the near-PIL areas and flare ribbons in observations and simulations (Figures 2 and 10), we find that the morphology of PILs has almost no bearing on the morphology of flare ribbons. Hence, while one can accept Schrijver (2007) contention that larger amounts of near-PIL flux indicate a greater likelihood of a larger flare, the spatial arrangement of the PIL does not substantively constrain ribbons' spatial distribution.

- *Magnetic fluxes:* We find strong statistical correlations between the flare peak X-ray flux and the flare ribbon and PIL fluxes (Figure 6a): Spearman correlation coefficient $r_s(I_{\rm X,peak}, \Phi_{\rm ribbon}) = 0.9$ and $r_s(I_{\rm X,peak}, \Phi_{\rm PIL}) = 0.6$, respectively in agreement with Kazachenko et al. (2017) analysis. While correlation between flare size and PIL flux is in line with Schrijver (2007) hypothesis that flare-productive ARs tend to have stronger PILs, it could reflect the fact that larger ARs have stronger PILs and hence host larger flares. The correlation between the peak X-ray flux and the corresponding AR quantities is weaker, ranging from $r_s(I_{\rm X,peak}, \Phi_{\rm AR}) = 0.3$ for full dataset ($n = 3137$, `RibbonDB`, Kazachenko et al. 2017) to $r_s(I_{\rm X,peak}, \Phi_{\rm AR}) = 0.6$ for `FlareMagDB` ($n = 40$).

- *Reconnection flux fractions:* We find moderate correlation between the flare peak X-ray flux and the fraction of AR magnetic flux participating in the flare, consistent with earlier results (Figure 6b).

- *Mean magnetic shears:* In both observations and simulations we find that the mean magnetic shear is strongest within PIL areas, decreasing gradually within ribbon and AR areas (Figure 6c): $\alpha(AR, rbn, PIL) = [10, 18, 26] \times 10^3 G \cdot deg$ for `RibbonDB` vs. $\alpha(AR, rbn, PIL) = [0.06, 0.13, 0.17] \times 10^3 G \cdot deg$ for ARMS. The peak X-ray flux is moderately correlated with the mean magnetic shear within the AR and is weakly correlated with the mean magnetic shear within ribbon and PIL areas.

- *Current density morphology:* Qualitatively, current density maps consist of thread-like and patchy structures that do not exhibit any regular shape and do not correlate with ribbon locations, flare and/or CME occurrence (Figure 12).

- *Total vertical currents:* We find that the total area-integrated unsigned vertical current is largest within AR areas decreasing gradually within ribbon and PIL areas (Figure 6d).

- *Net currents: Over entire active region*, we find that currents are neutralized, in agreement with earlier studies (orange symbols in Figure 7a):

$$(DC/RC)_{\rm AR} = 0. \tag{18}$$

  Over one polarity (positive or negative) currents are non-neutralized (blue symbols in Figure 7a):

$$(DC/RC)_{\rm AR,+} \approx -(DC/RC)_{\rm AR,-} \neq 0. \tag{19}$$

  The central part of the active region around the PIL has the highest net current decreasing gradually within ribbon and AR areas (see red, green and blue symbols, Figure 7a). We find that the net current within flare ribbons strongly correlates with the mean magnetic shear within the PIL (Figure 7b, $r_s = 0.7$) with the scaling relationship $|DC/RC| \propto 0.02\bar{\alpha}_{\rm PIL} + 0.9$, implying that current non-neutralization is a manifestation of the shear accumulation along the PIL in agreement with simulations (Török et al. 2014; Dalmasse et al. 2015).

- *Confined vs. eruptive flares:* We find that for a given peak X-ray flux, confined events have larger PIL fluxes and lower mean PIL shears and ribbon net currents than eruptive events (see △ vs. • in Figures 6a, c and d), in agreement with Liu et al. 2017; Avallone & Sun 2020. We also find that the CME speed has a strong correlation with the fraction of the AR that participates in the flare (Figure 8). In fact the flux ratio is the only variable that has a correlation coefficient with the CME speed above $r_s > 0.4$.

To summarize, following Welsch et al. 2009 "intensive-extensive" classification, our analysis suggests that while flare peak X-ray fluxes are guided by *extensive* magnetic field properties that scale with the AR size (like the total amount of magnetic flux that participates in the reconnection process, Bobra & Couvidat 2015), the CME speeds are guided by *intensive* properties that do not scale with the AR size (like the fraction between the reconnection flux and the AR flux, defined by the amount of overlying field, Bobra & Ilonidis 2016; Sun et al. 2015) with little dependence on the amount of mean PIL shear or net current.

This study is the largest-yet statistical analysis of the flare vector magnetic fields within flare-ribbon and PIL areas and the relationship with other flare and AR properties. Such a statistical approach is useful since it allows us to discover general laws that may be overlooked by individual case studies.

The `FlareMagDB` catalog is available online[2] in CSV and IDL sav file formats, along with maps of vector magnetic fields, magnetic shear, current densities, PIL and ribbon masks, and can be used for different types of quantitative studies in the future, from constraining the properties of the simulations to further detailed observation studies. For example, a comparison of magnetic field properties with presence of sigmoidal structures or filaments would be valuable to clarify the relationship between the coronal structures and the photospheric magnetic fields. Analysis of the outliers in the derived trends, for example, events with large magnetic shear and small net current and vice versa, would be interesting. Extension of this statistical work to a larger number of confined flares observed over a decade of SDO, including temporal evolution of the magnetic field properties over the flare (e.g. Sharykin et al. 2020; Barczynski et al. 2020), would allow us to further advance our understanding of solar eruption magnetism.

We thank the HMI team for providing us with the vector magnetic field SDO/HMI data. We thank Marc DeRosa and the AIA team for providing us with the SDO/AIA data. We thank US taxpayers for providing the funding that made this research possible. We acknowledge support from NASA LWS NNH17ZDA001N, 80NSSC19K0070, NASA 80NSSC18K1283-HSR, NASA ECIP NNH18ZDA001N (MDK), NASA LWS Award 80NSSC19K0072 (BTW), NASA award SV0-09020 (XS), NSF award 1848250 (XS), NASA HSR Award 80NSSC18K1283 (AS), and NASA Grand Challenges 996790 and 997022 (AS).

DATA: Dataset is available online at `http://solarmuri.ssl.berkeley.edu/~kazachenko/FlareMagDB/`

[2] http://solarmuri.ssl.berkeley.edu/ kazachenko/FlareMagDB/

REFERENCES

Antiochos, S. K., DeVore, C. R., & Klimchuk, J. A. 1999, ApJ, 510, 485

Aulanier, G., Janvier, M., & Schmieder, B. 2012, A&A, 543, A110

Aulanier, G., Török, T., Démoulin, P., & DeLuca, E. E. 2010, ApJ, 708, 314
Avallone, E. A., & Sun, X. 2020, ApJ, 893, 123
Barczynski, K., Aulanier, G., Janvier, M., Schmieder, B., & Masson, S. 2020, The Astrophysical Journal, 895, 18
Bobra, M. G., & Couvidat, S. 2015, ApJ, 798, 135
Bobra, M. G., & Ilonidis, S. 2016, ApJ, 821, 127
Canfield, R. C., Kazachenko, M. D., Acton, L. W., et al. 2007, ApJL, 671, L81
Carmichael, H. 1964, NASA Special Publication, 50, 451
Chen, J., Kliem, B., & Liu, R. 2019, in EGU General Assembly Conference Abstracts, EGU General Assembly Conference Abstracts, 10039
Chintzoglou, G., Zhang, J., Cheung, M. C. M., & Kazachenko, M. 2019, ApJ, 871, 67
Dahlin, J. T., Antiochos, S. K., & DeVore, C. R. 2019, ApJ, 879, 96
Dalmasse, K., Aulanier, G., Démoulin, P., et al. 2015, ApJ, 810, 17
DeVore, C. R., & Antiochos, S. K. 2008, ApJ, 680, 740
Fisher, G. H., Welsch, B. T., Abbett, W. P., & Bercik, D. J. 2010, ApJ, 715, 242
Georgoulis, M. K., Nindos, A., & Zhang, H. 2019, Philosophical Transactions of the Royal Society of London Series A, 377, 20180094
Georgoulis, M. K., Titov, V. S., & Mikić, Z. 2012a, ApJ, 761, 61
Georgoulis, M. K., Tziotziou, K., & Raouafi, N.-E. 2012b, ApJ, 759, 1
Gosain, S., & Venkatakrishnan, P. 2010, ApJL, 720, L137
Hirayama, T. 1974, SoPh, 34, 323
Hoeksema, J. T., Liu, Y., Hayashi, K., et al. 2014, SoPh, 289, 3483
Janvier, M. 2016, ArXiv e-prints, arXiv:1612.06513
Janvier, M., Démoulin, P., & Dasso, S. 2014, SoPh, 289, 2633
Karna, N., Savcheva, A., Gibson, S., et al. 2021, ApJ, 913, 47
Karpen, J. T., Antiochos, S. K., & DeVore, C. R. 2012, ApJ, 760, 81
Kazachenko, M. D., Canfield, R. C., Longcope, D. W., & Qiu, J. 2010, ApJ, 722, 1539
—. 2012, SoPh, 277, 165
Kazachenko, M. D., Lynch, B. J., Welsch, B. T., & Sun, X. 2017, ApJ, 845, 49
Kliem, B., Su, Y. N., van Ballegooijen, A. A., & DeLuca, E. E. 2013, ApJ, 779, 129
Kliem, B., & Török, T. 2006, Physical Review Letters, 96, 255002
Kliem, B., Zhang, J., Torok, T., & Chintzoglou, G. 2021, in 43rd COSPAR Scientific Assembly. Held 28 January - 4 February, Vol. 43, 997
Kontogiannis, I., Georgoulis, M. K., Guerra, J. A., Park, S.-H., & Bloomfield, D. S. 2019, SoPh, 294, 130
Kopp, R. A., & Pneuman, G. W. 1976, SoPh, 50, 85
Leka, K. D., Canfield, R. C., McClymont, A. N., & van Driel-Gesztelyi, L. 1996, ApJ, 462, 547
Lemen, J. R., Title, A. M., Akin, D. J., et al. 2012, SoPh, 275, 17
Li, T., Hou, Y., Yang, S., et al. 2020, The Astrophysical Journal, 900, 128
Li, T., Chen, A., Hou, Y., et al. 2021, The Astrophysical Journal Letters, 917, L29
Lin, P. H., Kusano, K., & Leka, K. D. 2021, ApJ, 913, 124
Liu, Y., & Schuck, P. W. 2012, ApJ, 761, 105
Liu, Y., Sun, X., Torok, T., Titov, V. S., & Leake, J. E. 2017, The Astrophysical Journal, 846, L6
Longcope, D., Beveridge, C., Qiu, J., et al. 2007, SoPh, 244, 45
Longcope, D. W., & Welsch, B. T. 2000, ApJ, 545, 1089
Lynch, B. J., Airapetian, V. S., DeVore, C. R., et al. 2019, arXiv e-prints, arXiv:1906.03189
Lynch, B. J., Antiochos, S. K., DeVore, C. R., Luhmann, J. G., & Zurbuchen, T. H. 2008, ApJ, 683, 1192
Lynch, B. J., Antiochos, S. K., Li, Y., Luhmann, J. G., & DeVore, C. R. 2009, ApJ, 697, 1918
Lynch, B. J., & Edmondson, J. K. 2013, ApJ, 764, 87
Lynch, B. J., Palmerio, E., DeVore, C. R., et al. 2021, ApJ, 914, 39
McClymont, A. N., & Fisher, G. H. 1989, Washington DC American Geophysical Union Geophysical Monograph Series, 54, 219
Moore, R. L., Sterling, A. C., Hudson, H. S., & Lemen, J. R. 2001, ApJ, 552, 833
Pesnell, W. D., Thompson, B. J., & Chamberlin, P. C. 2012, SoPh, 275, 3
Petrie, G. J. D. 2019, The Astrophysical Journal Supplement Series, 240, 11
Ravindra, B., Venkatakrishnan, P., Tiwari, S. K., & Bhattacharyya, R. 2011, ApJ, 740, 19
Savcheva, A., Pariat, E., McKillop, S., et al. 2016, ApJ, 817, 43
—. 2015, ApJ, 810, 96
Savcheva, A., Pariat, E., van Ballegooijen, A., Aulanier, G., & DeLuca, E. 2012b, ApJ, 750, 15
Savcheva, A., & van Ballegooijen, A. 2009, ApJ, 703, 1766
Savcheva, A. S., Green, L. M., van Ballegooijen, A. A., & DeLuca, E. E. 2012, ApJ, 759, 105
Savcheva, A. S., McKillop, S. C., McCauley, P. I., Hanson, E. M., & DeLuca, E. E. 2014, SoPh, 289, 3297
Savcheva, A. S., van Ballegooijen, A. A., & DeLuca, E. E. 2012a, ApJ, 744, 78
Scherrer, P. H., Schou, J., Bush, R. I., et al. 2012, SoPh, 275, 207
Schmieder, B., & Aulanier, G. 2018, Solar Active Region Electric Currents Before and During Eruptive Flares (American Geophysical Union (AGU)), 391–406
Schrijver, C. J. 2007, ApJL, 655, L117
Sharykin, I. N., Zimovets, I. V., & Myshyakov, I. I. 2020, The Astrophysical Journal, 893, 159

Sturrock, P. A. 1968, in IAU Symposium, Vol. 35, Structure and Development of Solar Active Regions, ed. K. O. Kiepenheuer, 471
Su, Y., Surges, V., van Ballegooijen, A., DeLuca, E., & Golub, L. 2011, ApJ, 734, 53
Sun, X., & Cheung, M. C. M. 2021, SoPh, 296, 7
Sun, X., Hoeksema, J. T., Liu, Y., Kazachenko, M., & Chen, R. 2017, ApJ, 839, 67
Sun, X., Bobra, M. G., Hoeksema, J. T., et al. 2015, ApJL, 804, L28
Titov, V. S., Mikic, Z., Linker, J. A., & Lionello, R. 2008, ApJ, 675, 1614
Toriumi, S., Schrijver, C. J., Harra, L. K., Hudson, H., & Nagashima, K. 2017, ApJ, 834, 56
Toriumi, S., & Wang, H. 2019, Living Reviews in Solar Physics, 16, 3
Torok, T., & Kliem, B. 2003, A&A, 406, 1043
Torok, T., Leake, J. E., Titov, V. S., et al. 2014, ApJL, 782, L10
Tschernitz, J., Veronig, A. M., Thalmann, J. K., Hinterreiter, J., & Pötzi, W. 2018, ApJ, 853, 41
Vemareddy, P. 2015, ApJ, 806, 245
Venkatakrishnan, P., & Tiwari, S. K. 2009, ApJL, 706, L114
Wall, J. V., & Jenkins, C. R. 2012, Practical Statistics for Astronomers
Wang, H., Liu, C., Ahn, K., et al. 2017, Nature Astronomy, 1, 0085
Warren, H. P., & Antiochos, S. K. 2004, ApJL, 611, L49
Welsch, B. T., Li, Y., Schuck, P. W., & Fisher, G. H. 2009, ApJ, 705, 821
Wheatland, M. S. 2000, ApJ, 532, 1209
Wyper, P. F., Antiochos, S. K., DeVore, C. R., et al. 2021, ApJ, 909, 54
Yashiro, S., Akiyama, S., Gopalswamy, N., & Howard, R. A. 2006, ApJL, 650, L143

APPENDIX

A. FLAREMAGDB FOR ALL EVENTS: MAGNETIC SHEAR AND VERTICAL CURRENT MAPS

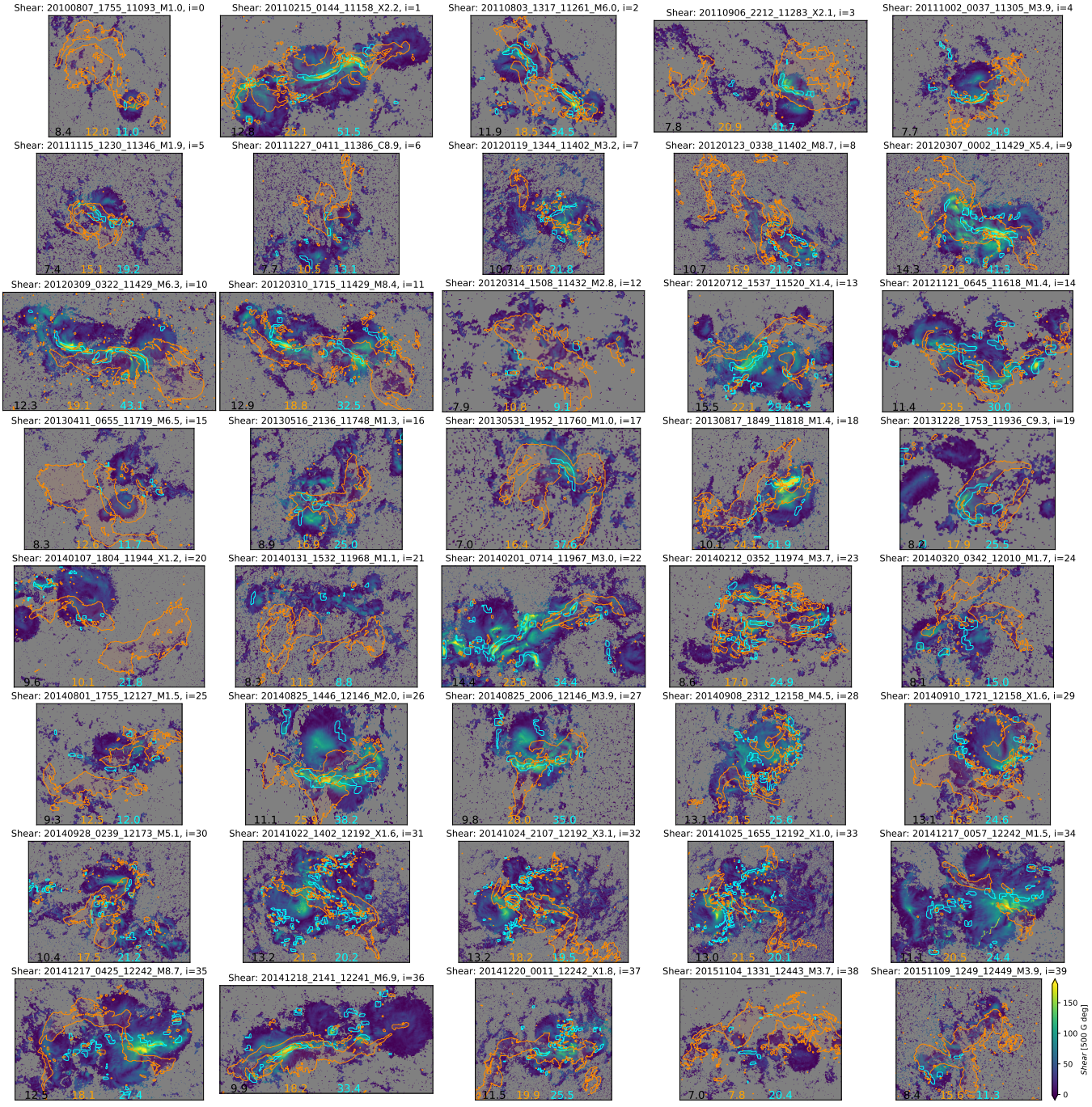

Figure 11. Magnetic field shear, α, for 40 events from the FlareMagDB database. Black, orange and cyan numbers indicate mean magnetic shear within AR, ribbon and PIL areas, respectively (see column $\bar{\alpha}$ in Table 1).

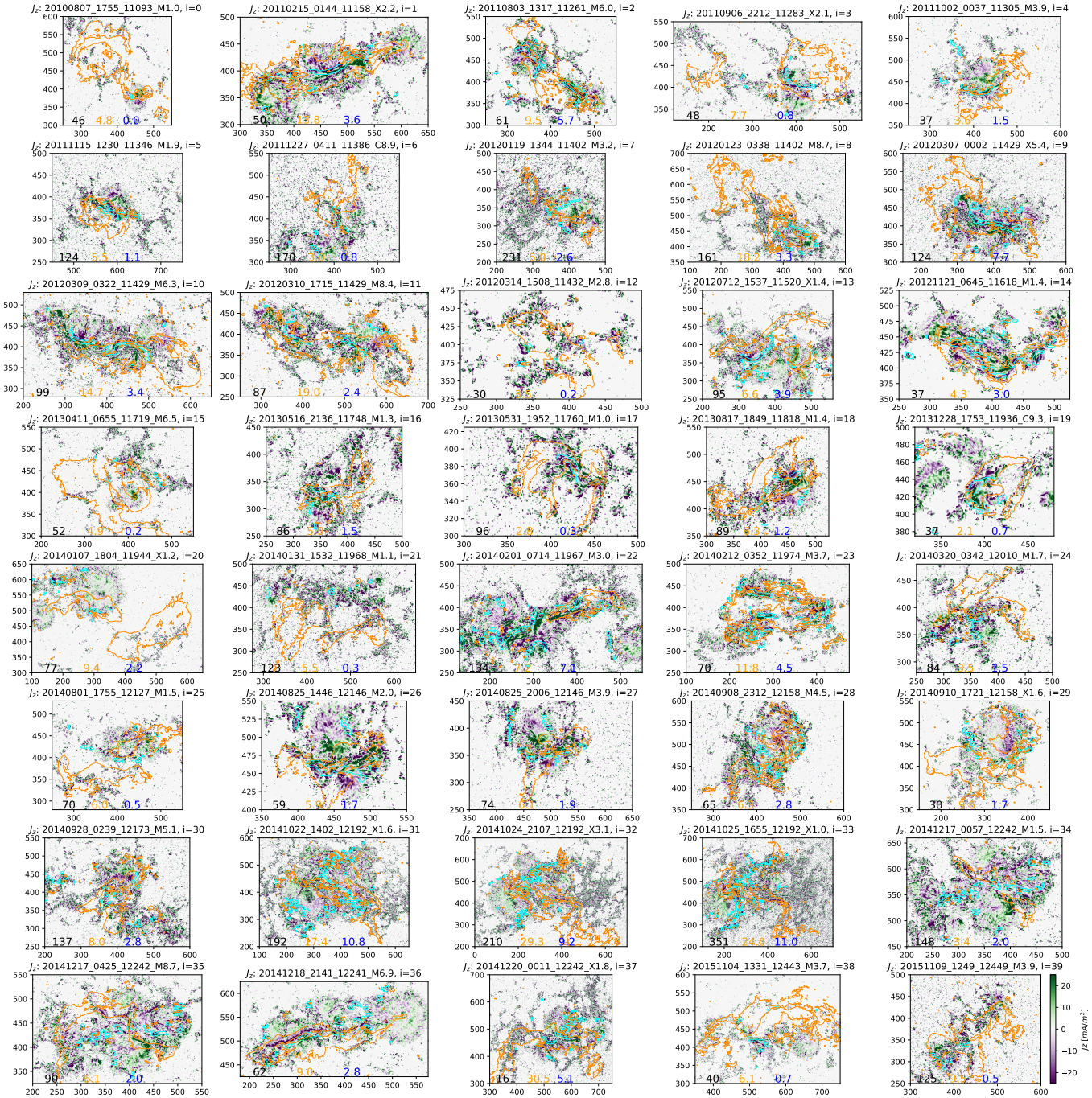

Figure 12. Vertical current distribution, J_z, for 40 events from the FlareMagDB database. Black, orange and blue numbers indicate total electric current within AR, ribbon and PIL areas, respectively (see column $I_{z,u}$ in Table 1).